THESIS

ANALYSIS OF LEAC BIOSENSOR FOR SCALABLE MANUFACTURING USING BPM AND FDTD SIMULATION METHODS

Submitted by

Cameron Dane Holmes

Department of Electrical and Computer Engineering

In partial fulfilment of the requirements

For the Degree of Master of Science

Colorado State University

Fort Collins, Colorado

Fall 2024

Master's Committee:

Advisor: Kevin L. Lear

Mahdi Nikdast
Matt Kipper

ABSTRACT

TOLERANCE ANALYSIS OF LEAC BIOSENSOR FOR SCALABLE MANUFACTURING USING BPM AND FDTD SIMULATION METHODS

The increasing demand for rapid, scalable, and accurate diagnostic tools has driven the development of optical biosensing technologies. LEAC (Local Evanescent Array-Coupled) biosensors, which leverage the evanescent field generated by optical waveguides, are particularly well-suited for applications in biomedical diagnostics, environmental monitoring, and point-of-care testing. LEAC biosensors have previously been fabricated in incomplete and unoptimized near-commercial CMOS processes and fully custom processes in a university cleanroom but have not been implemented in suitable high-volume processes such as commercial silicon photonics. A primary motivation for the research presented in this thesis is to evaluate the ability to fabricate LEAC biosensors operating at 1550 nm wavelengths in the commercial AIM Photonics' active silicon photonics process.

This thesis presents a comprehensive tolerance analysis of LEAC sensors for both bulk sample layers (400 nm thick) and protein monolayers (10 nm thick) in AIM's process, focusing on the impact of variations in key design parameters—specifically waveguide core thickness, cladding layers, and photodetector placement—on sensor sensitivity. Beam Propagation Method (BPM) and Finite-Difference Time-Domain (FDTD) simulation techniques are employed to assess how these tolerances affect optical field propagation, power dissipation, and flux into the photodetector, serving as proxies for sensor performance. Additionally, the study examines

crosstalk between multiple sensing regions, evaluating how refractive index variations in one region influence adjacent regions—an important consideration for multi-region sensors.

Results show that sensor sensitivity increases with cladding thickness and decreases with waveguide core thickness. A 25 nm manufacturing error in core thickness resulted in less than a 10% sensitivity shift, and a 300 nm cladding thickness error had a similarly small effect. Resonant absorption between the core and photodetector was observed across both bulk and monolayer samples. Sensitivity depends heavily on proximity to resonance; a 10% error in photodetector thickness at resonance caused a 600% change in sensitivity, while off-resonance, the same error had minimal impact. Coupled Mode Theory (CMT) explained these energy transfers and power fluctuations.

ANOVA analysis of full-device FDTD simulations quantified forward crosstalk due to modulated absorption from sample regions closer to the optical source (upstream). Forward crosstalk was found to be negligible for protein monolayer samples but could be significant in bulk samples. However, even in bulk samples, forward crosstalk was largely mitigated using photocurrent ratios with a reference region. A crosstalk ratio was used as a metric to determine the influence of each refractive index (n_1, n_3) on the photocurrent ratio. In the forward crosstalk direction, the use of photocurrent ratios decreased the magnitude of the forward crosstalk ratio; however, the use of photocurrents inherently introduces dependence on downstream indices (reverse crosstalk).

Reverse crosstalk, caused by reflections at the dielectric boundary between sensing regions, was found to be negligible using photocurrent ratios with bulk analytes; however, with monolayers, the use of photocurrent ratios introduced a slight dependence on the downstream region, indicating minor backward crosstalk. This can be mitigated by using raw current values

rather than current ratios. Raw currents eliminate backward crosstalk in region 1, while photocurrent ratios effectively eliminate forward crosstalk in region 3.

ACKNOWLEDGMENTS

I would like to express my deepest gratitude to my advisor, Kevin Lear, for his invaluable guidance, support, and encouragement throughout the course of my research. I am also immensely grateful to my committee members, Mahdi Nikdast and Matt Kipper, for their time, constructive suggestions, and commitment to my academic progress.

A heartfelt thank you goes to my family and friends for their unwavering love, patience, and support. Their belief in me has been a constant source of inspiration.

To my loving fiancée, thank you for your steadfast support and encouragement throughout this journey. Your love, patience, and belief in me have been a source of strength and motivation.

TABLE OF CONTENTS

CHAPTER 1 – INTRODUCTION

The search for rapid, accurate, and scalable diagnostic tools has intensified in recent years, driven by the growing demand for real-time health monitoring, environmental assessments, and chemical detection. Traditional diagnostic methods, such as enzyme-linked immunosorbent assays (ELISA) [1], are considered gold standards; however, their limitations in cost, time, and labor have spurred the development of advanced technologies. Optical biosensing has emerged as a promising alternative, offering label-free, real-time detection by leveraging the interaction between light and matter. These optical biosensors provide speed and sensitivity, making them indispensable in biomedical diagnostics, point-of-care (PoC) testing, and large-scale environmental monitoring systems.

Among the various optical biosensing technologies, Local Evanescent Array Coupled (LEAC) biosensors stand out for their ability to detect minute changes in the refractive index. Historically, these sensors have employed silicon nitride (SiN) or similar materials as the core waveguide, enabling operation at visible wavelengths. The challenge with earlier designs was not in the material itself, but in their reliance on incomplete or unoptimized CMOS processes, where SiN was repurposed from its original use in electronics. This configuration was effective for early implementations, but challenges arose as these designs were not fully compatible with modern high-volume, silicon photonics manufacturing processes.

In recent years, the focus has shifted to more scalable designs that leverage modern silicon photonics fabrication processes, where waveguides are a standard component, fully integrated with high-volume production. While silicon nitride (Si_3N_4) or similar materials have been used in the past, the key advancement lies in the optimization of the operating wavelength, such as the shift to 1550 nm, which requires photodetectors made from materials like germanium (Ge). This shift, along with the push to fully integrate LEAC biosensors into modern fabrication processes, has significantly advanced the field,

enhancing both sensitivity and compatibility with current manufacturing standards.

The sensing mechanism in LEAC biosensors relies on the evanescent field generated by the optical waveguide. This field, which extends into the surrounding medium, is highly sensitive to changes in the refractive index of nearby materials. The interaction between this evanescent field and the surrounding environment forms the basis of the biosensing process. The strength and sensitivity of the evanescent field depend heavily on critical design parameters, such as the thickness of the waveguide core and cladding layers, as well as the placement and properties of the photodetector. Optimizing these parameters is essential for enhancing the performance of modern LEAC biosensors.

One of the key advantages of LEAC biosensors is their ability to incorporate multiple sensing regions on a single waveguide. This versatility enables simultaneous detection of multiple analytes or sample regions, significantly improving the throughput of the sensor.

1.1 Thesis Goals and Overview

This thesis explores how layer thickness tolerances—specifically in the waveguide core, cladding, and photodetector layers—affect LEAC biosensor performance using Beam Propagation Method (BPM) and Finite-Difference Time-Domain (FDTD) simulations. By analyzing the impact of these tolerances on sensor sensitivity, this study aims to inform the design of future LEAC biosensors. Additionally, this work investigates crosstalk between sensing regions, examining how refractive index variations in one region may affect sensing signals from adjacent regions—a critical factor for multi-region sensors. The study also addresses mode beating between the waveguide and photodetector, a phenomenon that causes power oscillations and impacts overall sensor performance.

This study aims to conduct a comprehensive tolerance analysis of the LEAC biosensor, focusing on the relationship between key device parameters, such as waveguide core thickness, photodetector thickness, and their separation. By analyzing how these parameters affect sensor sensitivity, the study seeks to optimize LEAC biosensor designs. Additionally, it investigates crosstalk between sensing regions, shedding light on how refractive index variations in one region influence adjacent areas. Notably,

this study uncovers complex mode beating between the waveguide and photodetector, resulting in power oscillations. Using Coupled Mode Theory (CMT), the energy transfer and power fluctuations between these structures are modeled to better understand how design parameters influence sensor performance.

In the introductory section, a detailed overview of the LEAC biosensor is provided, along with a brief introduction to guided optics. Chapter 2 presents a literature review that highlights the current state of the art and establishes the motivation for this study. Chapter 3 outlines the methodology, focusing on the simulation techniques used, including Beam Propagation Method (BPM) and Finite-Difference Time-Domain (FDTD). Chapter 4 presents the results of these simulations, with an emphasis on the influence of layer thickness on sensor sensitivity and performance. Chapter 5 discusses the results of the full device simulation, particularly addressing crosstalk between multiple sensing regions. Chapter 6 applies Coupled Mode Theory (CMT) to explain observed resonance phenomenon and explore energy transfer between modes. Finally, Chapter 7 concludes the thesis with a discussion of key findings and recommendations for future research.

1.2 LEAC Biosensor: Design and Operation

The Local Evanescent Array-Coupled (LEAC) sensor is typically a non-resonant optical waveguide sensor with several unique advantages over conventional biosensors. Unlike resonant sensors, which operate near a fixed optical frequency, LEAC sensors can operate over a wide range of wavelengths, making them adaptable to various sensing conditions. This flexibility allows LEAC sensors to be used with either LED or laser sources, increasing their practicality.

A defining feature of LEAC biosensors is their ability to integrate multiple sensing regions on a single waveguide. These regions are isolated yet share the same optical waveguide, reducing sensor array complexity and enabling high-volume applications. LEAC sensors function as self-contained platforms, eliminating the need for off-chip equipment for signal transduction, thus reducing system size and cost. These properties make LEAC biosensors ideal for point-of-care diagnostics and portable environmental monitoring.

Initial LEAC devices have been fabricated using both a non-optimized CMOS process [2] and a custom university fabrication process [3], demonstrating basic functionality. However, challenges arise when transitioning to large-scale production. This thesis focuses on addressing these challenges by analyzing manufacturing tolerances—especially the core thickness, cladding layers, and photodetector placement—which are crucial for consistent, repeatable performance.

The following chapter reviews the current state of optical biosensing technologies, focusing on LEAC biosensors. The review identifies key gaps, particularly in the understanding of manufacturing tolerances and their impact on sensor performance, which motivates the research presented in this thesis

CHAPTER 2 – LITERATURE REVIEW

Traditional laboratory detection techniques, such as enzyme-linked immunosorbent assay (ELISA), while effective, are often costly, labor-intensive, and time-consuming [1]. In contrast, optical biosensing technologies have emerged as a promising alternative, offering real-time, label-free, and highly sensitive detection methods that meet the growing demands of biomedical, environmental, and chemical applications. These sensors exploit the interaction between light and biological samples, detecting changes in refractive index, fluorescence, molecular binding events, or other optical properties that correlate with the presence or concentration of target analytes. Their rapid, decentralized diagnostic capability makes them ideal PoC testing, which is essential in public health contexts where timely diagnostics can significantly impact patient outcomes and disease management, as seen during the COVID-19 pandemic and other public health emergencies [4].

This chapter provides a review of various optical biosensing platforms, with a particular emphasis on silicon photonic biosensors and their inherent advantages in terms of scalability, integration, and sensitivity. Primary optical biosensing platforms, including Surface Plasmon Resonance (SPR) and interferometric biosensors, are discussed in detail, with attention to their operational principles and limitations. These limitations—particularly in scalability, sensitivity to environmental conditions, and material costs—restrict their use in large-scale and decentralized applications, such as PoC testing. The discussion then shifts to silicon photonic biosensors, which overcome many of the challenges faced by traditional optical sensing platforms. Among these, Local Evanescent Array Coupled (LEAC) biosensors represent a significant advancement. Leveraging the scalability of silicon photonics and the sensitivity of evanescent fields, LEAC biosensors offer a highly sensitive, stable, low-cost, and scalable solution for biosensing applications.

Finally, the critical role of tolerance analysis in the fabrication of LEAC biosensors is addressed. This study aims to assess the impact of manufacturing tolerances on the performance and reliability of

these devices, underscoring the importance of precise fabrication techniques in ensuring consistent sensor performance.

2.1 Overview of Optical Biosensing

Optical biosensing technologies leverage the interaction between light and biological systems to detect specific analytes, offering several distinct advantages over traditional methods like ELISA and polymerase chain reaction (PCR). These biosensors can provide real-time, label-free detection, significantly reducing the time and resources required for accurate diagnostics.

The core principle behind optical biosensing lies in the modulation of light properties, such as intensity, phase, wavelength, or polarization, upon interaction with a target analyte. These changes are then translated into measurable signals that correspond to the presence or concentration of biological molecules, such as proteins, DNA, or pathogens. Optical biosensors are especially sensitive to minute changes in refractive index, enabling them to detect molecular binding events with high precision.

Several platforms are commonly used in optical biosensing, each with unique mechanisms and applications; however, each is subjected to its own set of constraints and limitations that impede its scalability and environmental sensitivity. Common technologies include SPR, interferometric biosensors, and silicon photonic structures such as waveguide biosensors and the LEAC biosensor. In PoC testing environments, scalability and robustness to environmental variations, such as temperature fluctuations or humidity, are critical factors that affect the performance and reliability of these sensors.

2.1.1 Surface Plasmon Resonance (SPR)

SPR has emerged as a highly sensitive and widely adopted method for chemical and biological sensing, offering real-time, label-free detection. This technique leverages the resonance effect that arises from the interaction of electromagnetic waves at the interface between a dielectric medium and a thin metal film, typically gold. SPR is sensitive to minute changes in the refractive index, and modern SPR systems achieve bulk sensitivities on the order of 10^{-7} refractive index units (RIU) and surface sensing capabilities as fine as $1\ \mathrm{pg/mm^2}$ [5]. However, despite its impressive sensitivity and widespread use, several challenges restrict the broader adoption of SPR technology.

While advancements in light sources have been pivotal in improving SPR performance, they alone cannot address many of the technology's inherent limitations. As Prabowo et al. have emphasized, monochromatic light sources such as laser diodes enable precise angular interrogation, enhancing sensitivity, but often come with high costs and complex alignment requirements [6]. Conversely, polychromatic sources, like LEDs, allow for versatile wavelength interrogation and broaden the potential for spectral analysis. However, this versatility introduces trade-offs in sensitivity and resolution, complicating the development of universally applicable SPR systems. Despite attempts to lower costs by integrating solid-state light sources such as LEDs and OLEDs, the high cost of noble metals like gold remains a significant barrier to reducing the overall price of SPR sensors. Gold, though critical for maintaining SPR sensitivity, is expensive and difficult to scale for mass production. Efforts to develop disposable SPR platforms may offer a partial solution, but the precision required in fabrication to maintain sensitivity limits large-scale, affordable deployment.

The miniaturization of SPR systems, particularly for PoC applications, presents additional hurdles. Portable SPR systems necessitate complex optical setups to effectively couple light and excite the surface plasmon (SP) mode [4, 5]. Moreover, the dielectric coupler metal, and analyte all exhibit dependence on the ambient temperature, affecting the resonance of the device [6]. This makes SPR systems susceptible to environmental fluctuations, further complicating their use in field applications where precise temperature control may not be feasible. Another challenge lies in the durability and long-term stability of SPR sensors, which are largely dependent on the metal films used—primarily gold. These films are prone to degradation, especially in harsh or reactive environments, leading to performance declines over time [5].

Despite the significant advancements in SPR technology, including improvements in light sources and efforts toward miniaturization, key limitations remain. The high cost of materials, intricate fabrication requirements, and the performance trade-offs in portable systems pose substantial barriers to widespread SPR adoption, particularly in PoC diagnostics.

2.1.2 Interferometric Biosensors

Interferometric biosensors are highly sensitive optical devices that detect changes in the refractive index by utilizing the interference of light waves. Various interferometer architectures have been developed, each offering unique advantages and limitations. Common designs include the Mach-Zehnder Interferometer (MZI) and the Young Interferometer, which have been miniaturized to operate using photonic waveguides. In these configurations, the evanescent field penetrates the surrounding medium, and any change in the bulk refractive index or adsorption in the biological layer induces a phase shift in the propagating light wave. By comparing this phase-shifted light to a reference wave, an interference pattern is generated, revealing important biochemical interactions occurring on the sensor's surface [4].

Photonic-based interferometric biosensors have achieved remarkable sensitivity levels comparable to SPR. For example, in the MZI, light is divided into two arms: one arm interacts with the analyte, while the other serves as a reference. The interference pattern produced when the two beams are recombined provides detailed information about molecular interactions on the sensor's surface. Bulk detection limits as low as 7×10^{-6} RIU have been reported [7]. Similarly, the Young Interferometer offers an alternative architecture in which light passing through both a sensing and reference arm generates far-field interference patterns. This design helps mitigate sensitivity fading caused by intensity variations, enabling the measurement of molecular interactions with high precision. Recent advances in dual-polarization interferometry have further enhanced Young interferometry, providing real-time, label-free detection of biomolecular interactions at the nanoscale, with bulk sample sensitivities reaching 9×10^{-9} RIU and surface detection limits of $13.0\ \mathrm{fg\ mm^{-2}}$ [8].

While these technologies demonstrate impressive sensitivity and benefit from the scalability of photonic integrated circuit platforms, significant challenges remain that hinder broader adoption for PoC testing. These challenges include environmental sensitivity, fabrication complexities, and the high cost of precise manufacturing. One of the most prominent issues is the need for monochromatic sources to maintain a long enough coherence length to achieve effective interference. Such laser sources contribute substantially to the overall cost of the device. Additionally, these sources often require temperature

stabilization, necessitating additional infrastructure for the device to operate reliably [5, 8]. Overcoming these hurdles will be crucial for the larger-scale implementation of interferometric biosensors in clinical and industrial settings.

2.1.3 Resonator Biosensors

Resonator-based biosensors operate on the principle of light confinement within an optical cavity, where the light repeatedly oscillates due to constructive interference. These sensors rely on the resonance effect, where only specific wavelengths of light, called resonance frequencies, can propagate without significant losses [9]. When an analyte binds to the sensor's surface, it induces a change in the refractive index near the resonator. This interaction shifts the resonance frequency, which can be measured to detect the presence and concentration of the analyte with high sensitivity.

The most common types of resonator biosensors include microring resonators, whispering gallery mode (WGM) resonators, and Fabry-Pérot (FP) cavities. Microring resonators are small, donut-shaped devices where light circulates in a circular path. WGM resonators, such as microspheres or microdisks, confine light through total internal reflection along their boundaries. Fabry-Pérot cavities, though less common in compact biosensors, consist of two parallel mirrors that reflect light back and forth, creating resonance based on cavity length [9].Recent developments, particularly in microring resonators, have achieved sensitivities up to 112 nm/RIU, as seen in silicon oxynitride-based devices. In volumetric sensing, resonators can detect changes in refractive index as small as 1.6×10^{-6} RIU [10] This level of sensitivity makes them highly effective for detecting small biomolecules, proteins, and toxins in applications such as environmental monitoring, clinical diagnostics, and food safety.

Beyond their high sensitivity, resonator-based biosensors also offer scalability and potential for integration with existing semiconductor technologies. These devices are typically fabricated using standard CMOS processes, allowing for the mass production of biosensors at a relatively low cost. Additionally, the ability to multiplex—detecting multiple analytes simultaneously—further enhances their practicality, particularly for diagnostic applications. The compact size of microring resonators makes

them ideal for integration into portable devices, such as wearable sensors or handheld diagnostic tools, providing flexible and accessible solutions for real-time monitoring and diagnostics.

Despite their many advantages, resonator-based biosensors face several limitations. A key challenge is the trade-off between the quality factor (Q-factor) and sensitivity. As resonator size decreases for higher sensitivity, the Q-factor often drops, reducing measurement precision. Additionally, resonators are highly sensitive to temperature fluctuations, which can cause refractive index shifts, leading to false positives or inaccurate readings. Silicon, a common material in photonics, has a high positive thermo-optic coefficient ($\sim 1.8 \times 10^{-4}/°C$) [11], requiring temperature compensation mechanisms like calibration or thermal insulation, which adds complexity and power consumption to the design.

2.1.4 Local Evanescent Array Coupled (LEAC) Biosensors

Local Evanescent Array Coupled (LEAC) biosensors represent a hybrid biosensing approach that integrates the sensitivity of evanescent field-based detection with the scalability and integration potential of silicon photonics. The fundamental principle of LEAC biosensors is based on the interaction between light propagating through a waveguide and the surrounding medium. The evanescent field, which extends from the waveguide into the adjacent environment, interacts with nearby molecules [12]. When analytes bind to the sensor surface, they alter the local refractive index, resulting in a measurable shift in the optical signal.

In a LEAC system, multiple sections of a waveguide are arranged in a sequential array, each functioning as an independent sensor. The waveguide couples light into the sensing regions, where molecular binding events occur, and the resulting changes in the refractive index are detected through shifts in the evanescent field. These shifts are dependent on the concentration and refractive index of the analytes, allowing for highly sensitive detection. LEAC biosensors are also designed with a reference section, which provides a stable control measurement to improve accuracy and compensate for environmental variations.

The sensitivity of LEAC biosensors is one of their key strengths. The technology has demonstrated sensitivity to refractive index changes on the order of 4.6×10^{-6} RIU in static measurements, with real-time sensitivity reaching 4.1×10^{-5} RIU [13]. This high level of sensitivity is comparable to, and in some cases exceeds, that of traditional Surface Plasmon Resonance (SPR) systems, making LEAC biosensors well-suited for detecting small molecular interactions. Furthermore, LEAC biosensors have been shown to detect biomolecular interactions in real-time, allowing for dynamic monitoring of processes such as protein binding or DNA hybridization.

LEAC biosensors are highly robust against environmental factors like temperature and humidity fluctuations, making them ideal for point-of-care (PoC) diagnostics where conditions are less controlled. By integrating a reference region and leveraging silicon photonic fabrication, LEAC sensors minimize scattering and absorption losses, ensuring high performance in diverse environments. However, they face challenges such as fabrication imperfections, which can introduce noise and reduce reproducibility [13]. Additionally, temperature-induced shifts in refractive index require careful calibration, adding complexity to device design. Despite these limitations, LEAC biosensors offer a sensitive, scalable, and cost-effective solution for biosensing, combining the strengths of evanescent field detection with the scalability of silicon photonics, making them a strong candidate for future diagnostic technologies

2.2 Tolerance Analysis in Optical Biosensing

Tolerance analysis is essential in assessing the impact of manufacturing and environmental variations on the performance of biosensors, particularly for point-of-care (PoC) applications where reliability and consistency are paramount. In LEAC biosensors, the device's sensitivity and robustness are heavily influenced by factors such as fabrication imperfections, surface roughness, and variations in waveguide geometry, all introducing signal noise and degrading performance. The precise control over these parameters is critical for achieving accurate, reproducible measurements across different production batches.

Ardoino et al. (2024) provide a detailed study on microring resonator (MRR)-based biosensors, highlighting key challenges in optimizing surface functionalization, which plays a critical role in the

sensor's ability to detect low-abundance biomarkers [14]. The study emphasizes the importance of minimizing surface roughness and controlling the silanization process to ensure uniformity across the biosensor surface. Even minor deviations in surface roughness, caused by inconsistent plasma treatments or variations in silane concentration, resulted in significant changes in detection sensitivity. This finding underscores the necessity of stringent control over surface preparation and functionalization during manufacturing to mitigate tolerance-related issues and maintain sensor performance.

Huraiya et al. (2024) extend this discussion by examining the fabrication tolerance of a novel V-shaped photonic crystal fiber (PCF)-based surface plasmon resonance (SPR) sensor. Their study focuses on the impact of variations in critical structural parameters such as air-hole diameter, channel depth, and pitch on the sensor's performance. The sensor exhibited a tolerance of 5% for pitch and 10% for air-hole diameters, with a channel depth tolerance of ±2% [15]. Even slight deviations in these parameters resulted in significant changes in confinement loss and resonance wavelength, with a 10% increase in air-hole diameter leading to an 18.78 dB/cm increase in loss. These findings highlight the sensitivity of biosensor performance to geometric imperfections and the need for precision in fabrication processes to ensure consistency across production batches.

In both studies, the emphasis is placed on the critical need for tight control over fabrication processes and environmental conditions to minimize performance degradation due to tolerance-related variations. For PoC applications, where sensors must consistently deliver reliable results in non-ideal conditions, maintaining these tolerances becomes even more challenging. Therefore, ensuring robustness in manufacturing processes through tolerance analysis is key to producing high-performance biosensors capable of detecting low-concentration analytes with high sensitivity and repeatability.

In the case of LEAC biosensors, tolerance analysis becomes particularly important due to the complex interplay between the waveguide core, cladding layers, and the photodetector. Variations in the thickness of these layers can significantly affect the evanescent coupling, a crucial mechanism in LEAC designs that drives their high sensitivity. For instance, small deviations in waveguide core thickness can either enhance or severely diminish the coupling efficiency between the waveguide and the photodetector,

leading to variations in sensor output. Additionally, manufacturing imperfections in the photodetector itself, such as variations in thickness or material composition, can introduce resonances that affect the device's ability to detect subtle changes in the refractive index of the sensing region. This makes precise control over fabrication tolerances essential for achieving optimal sensor performance in LEAC-based biosensors.

2.3 Comparative Analysis of Optical Biosensing Technologies

In this section, we summarize the key optical biosensing technologies discussed throughout this chapter, providing a comparative analysis based on their performance metrics, scalability, sensitivity, and potential for integration into point-of-care (PoC) applications. This comparison highlights the advantages and limitations of each platform, offering insights into their suitability for different applications.

Table 2.1: Comparison of optical biosensing technology in terms of sensitivity, scalability, and current PoC limitations.

Technology	Bulk Sensitivity	Surface Sensitivity	Key device external dependencies	Scalability Limitations
SPR	10^{-7} RIU	1 pg mm^{-2}	• Highly sensitive to temperature fluctuations • Requires precise noble metal films	• Requires complex alignment and temperature stabilization
Interferometric Biosensor	10^{-9} RIU	13.0 fg mm^{-2}	• Sensitive to fabrication errors, temperature, and coherence length of light source	• External coherent light source and temperature stabilization
Resonance Biosensor	Up to 112 nm/RIU	–	• Sensitive to temperature and refractive index shifts, requires high Q-factor for precision	• Tight manufacturing tolerances and temperature stabilization
LEAC Biosensor	4.6×10^{-6} RIU	–	• Sensitive to waveguide core and photodetector thickness, robust against environmental fluctuations	• Requires precise fabrication

Surface Plasmon Resonance (SPR) remains one of the most sensitive platforms, capable of detecting minute changes in refractive index, making it ideal for detailed molecular interactions. However, its practical application in point-of-care (PoC) diagnostics is limited due to several factors, including environmental sensitivity, reliance on expensive materials like gold, and complex coupling setups. The scalability of SPR systems is also hindered by their requirement for precise alignment and temperature stabilization, making mass production and portability challenging, as reflected by its high sensitivity to fabrication and environmental dependencies.

Interferometric biosensors, such as the Mach-Zehnder and Young interferometers, offer similar sensitivity to SPR but are similarly constrained by their need for precise laser sources and tight temperature control. While these systems can be miniaturized using silicon photonics, the fabrication complexity and environmental sensitivity continue to present significant hurdles, particularly in decentralized or field applications where temperature fluctuations are common.

Microring resonators, with their high sensitivity and compatibility with standard CMOS processes, present a more scalable alternative. These devices offer promising applications in PoC diagnostics due to their compact size and potential for integration into portable devices. However, resonator-based biosensors are highly dependent on maintaining a precise balance between the Q-factor and sensitivity, making them vulnerable to temperature-induced shifts in resonance wavelengths, which can affect measurement accuracy. This sensitivity to environmental variations introduces additional challenges in fabrication and operational stability.

Local Evanescent Array Coupled (LEAC) biosensors effectively bridge the gap between high sensitivity and scalability. By leveraging silicon photonics, LEAC biosensors offer cost-effective fabrication and exhibit robustness against environmental factors such as temperature and humidity fluctuations. The integration of reference waveguides for calibration further enhances their reliability, especially in PoC diagnostics where environmental conditions are less predictable. However, maintaining precise fabrication tolerances—particularly in the waveguide core and photodetector—is critical to

ensuring consistent performance across large production batches, underscoring the importance of manufacturing precision for this technology.

This comparison highlights the trade-offs between sensitivity, scalability, and environmental robustness in each platform, as summarized in the table. While all these technologies offer high-performance sensing capabilities, their practical applications, especially in decentralized settings, depend heavily on how well they balance these factors.

2.4 Conclusion

In this chapter, we explored the diverse landscape of optical biosensing technologies, focusing on their applications, limitations, and potential for point-of-care (PoC) diagnostics. Traditional platforms like Surface Plasmon Resonance (SPR) and interferometric biosensors demonstrate impressive sensitivity but are hindered by challenges in scalability, environmental sensitivity, and fabrication complexity. Microring resonators offer a more scalable alternative but remain sensitive to environmental fluctuations, particularly temperature changes.

Local Evanescent Array Coupled (LEAC) biosensors stand out by combining the scalability of silicon photonics with the high sensitivity of evanescent field detection, making them well-suited for PoC applications. However, achieving consistency across large-scale production relies heavily on precise fabrication processes and effective tolerance analysis. By comparing these technologies, we emphasize the importance of balancing sensitivity, environmental robustness, and manufacturing precision to meet the growing demands of decentralized diagnostic applications.

The following chapter will delve into the simulation methods used for tolerance analysis, including Beam Propagation Method (BPM) and Finite-Difference Time-Domain (FDTD), to evaluate how variations in waveguide geometry and photodetector placement impact the performance and sensitivity of LEAC biosensors.

CHAPTER 3 – OPTICAL SIMULATION METHODS

In this study, two distinct simulation algorithms were employed to conduct a comprehensive analysis of the LEAC biosensor's structure and performance, focusing on both individual sensing regions and the complete multi-region device. Understanding the underlying numerical methods is crucial for appreciating the study's limitations and nuances. The Beam Propagation Method (BPM), utilized within the Synopsis RSoft suite, provides a rapid and high-quality approximation of waveguide mode behavior by solving the Helmholtz equation typically in the forward direction. In contrast, the Finite Difference Time Domain (FDTD) method directly solves Maxwell's equations over both space and time, offering a detailed simulation of electromagnetic wave propagation with fewer approximations than BPM. While comprehensive, the FDTD algorithm is computationally intensive, creating limitations on the domain and size of devices that can be simulated. This chapter provides a detailed description of both algorithms, highlighting their specific limitations and nuances.

3.1 Beam Propagation Method

The Beam Propagation Method (BPM) computes numerical solutions to an approximated version of the wave equation for monochromatic light propagating within limited angles. A tolerance analysis was conducted in this study using semi-vectorial, one-directional BPM. Traditionally, BPM solves the Helmholtz equation for a scalar field, though advancements have enabled more complex treatments that account for the vectorial nature of light. For clarity and simplicity, this discussion primarily focuses on the scalar case that would apply to free space propagation of light, such as what would be modeled for optical interconnects between satellites in orbit of the Earth.

3.1.1 Helmholtz Equitation and Scalar Fields

The Helmholtz equation, which governs wave propagation, is given by (see appendix A for derivation of the wave equation) [16]:

$$\nabla^2\psi + k_0^2 n^2(x,y,z)\psi = 0 \tag{3.1}$$

Where:

- $\psi(x, y, z)$ is the spatially dependent field
- k_0 is the wavenumber in free space
- $n(x, y, z)$ is the refractive index profile of the medium.

The spatially dependent electric field can then be written as:

$$E(x, y, z, t) = \psi(x, y, z)e^{-i\omega t} \tag{3.2}$$

where ω is the monochromatic angular frequency. To this point, the equation is the exact solution to a scalar field. In a guided wave scenario, the field ψ varies spatially most rapidly along the propagation direction z, while its variation in the transverse (x, y) plane is relatively slow since the angle of light propagation is closer to the z-direction than the orthogonal axes, i.e. is paraxial. To account for this, the field can be separated into two components:

$$\psi(x, y, z) = u(x, y, z)e^{i\beta z} \tag{3.3}$$

where β is the rate at which the phase of the wave changes along the z-direction, determining how quickly the wave oscillates or progresses spatially in that direction. Substituting equation 3.3 into 3.1 and simplifying, we obtain:

$$\frac{d^2u}{dz^2} - 2i\beta\frac{du}{dz} + \frac{d^2u}{dx^2} + \frac{d^2u}{dy^2} + (k^2 - \beta^2) = 0 \tag{3.4}$$

The paraxial approximation assumes that the variation of u with respect to z sufficiently slow, allowing us to simplify the equation further by considering only the first-order variation of u in z. Applying this approximation, the second-order term is neglected, leading to the paraxial wave equation:

$$\frac{du}{dz} = \frac{i}{2\beta}\left[\frac{d^2u}{dx^2} + \frac{d^2u}{dy^2} + (k^2 - \beta^2)\right] \tag{3.5}$$

This is the scalar three-dimensional BPM equation. Given a spatial field of the form $\psi(x, y, z = 0)$ as an input, the above equation determines the spatial field for $z > 0$. While BPM is a powerful tool for modeling optical waveguides, its advantages and limitations must be noted. The method benefits from computational efficiency due to the separation of the rapidly varying phase along the z-direction, which

allows for coarser sampling along this direction. However, the limitations of BPM arise from the paraxial approximation, which assumes a slowly varying field along z. This approximation restricts the method's ability to handle large variations in the refractive index and limits propagation angles. Additionally, a significant limitation of BPM is its reliance on a purely positive propagation constant β, which simplifies the modeling process but can be inadequate for accurately representing back reflections at dielectric boundaries. This restriction arises because BPM assumes a constant β along the propagation direction, which does not account for scenarios where the effective index changes substantially. Consequently, BPM may not capture the full effects of back propagation or reflections in structures with significant variations in the propagation constant. For more accurate modeling of these effects, alternative methods such as FDTD, which do not rely on this assumption, can be more effective

3.1.2 Vectorial BPM

The limitations of BPM discussed in Section 3.1.1 are generally applicable; however, more advanced formulations can address or mitigate these limitations. A significant drawback of scalar BPM is its inability to account for the polarization of the mode, such as transverse electric (TE) versus transverse magnetic (TM) modes. To accurately model the loss associated with each polarization, the electric field must be treated as a vector rather than a scalar field. This is achieved by starting the BPM approximation with the vector wave equation instead of the scalar Helmholtz equation [17]. When applying the paraxial approximation to the fully vector wave equation, coupled fields that vary with respect to one another must be considered. Alternatively, a semi-vectorial approach can be used when only one polarization is present in the simulation. This approach reduces complexity and simulation time while still preserving the essential characteristics of wave polarization. All simulation in this study were completed using a semi-vectorial approach as the device is best suited for TE polarizations. Photonic integrated circuits (PICs) typically utilized guided modes, requiring the consideration of polarization.

3.1.3 Bi-Direction BPM

The issue of addressing back reflections is a fundamental limitation in BPM due to the paraxial approximation, which eliminates higher-order derivatives of ψ with respect to z. To correct this limitation, several methods can be employed, one of the most common being the bi-directional BPM approach. This method treats the forward and backward propagation of light in the waveguide as coupled equations that are solved simultaneously [18]. The core concept involves using a transfer matrix to manage both forward and backward propagation. This results in an equation:

$$\begin{bmatrix} \psi_{out}^{+} \\ \psi_{out}^{-} \end{bmatrix} = M \begin{bmatrix} \psi_{in}^{+} \\ \psi_{in}^{-} \end{bmatrix} \tag{3.6}$$

Where M is the transfer matrix for the entire structure, ψ_{in} is the inputted field and "+/-" denotes the direction of propagation. Considering an inputted field propagating down the waveguide (ψ_{in}^{+}), the model then iteratively solves for ψ_{in}^{-} by trying assuming that $\psi_{out}^{-} = 0$.

3.2 Finite Difference Time Domain

The Finite Difference Time Domain (FDTD) method is a widely used numerical technique for solving Maxwell's equations in both time and space. Unlike the Beam Propagation Method (BPM), which simplifies the problem by assuming a slowly varying deviation from a simple plane wave in a single propagation direction, FDTD provides a more comprehensive analysis by directly solving the wave equation derived from Maxwell's equations without approximations or simplifications. This method is particularly useful for simulating complex electromagnetic interactions and analyzing phenomena that involve time-dependent fields.

3.2.1 Maxwell's Equations and Hyperbolic Equations

In the FDTD method, Maxwell's equations are solved as a set of coupled partial differential equations (PDEs) that describe the behavior of electric and magnetic fields over time and space. These equations are [19,20]:

$$\nabla \times \vec{E}(\vec{r}, t) = -\mu_0 \frac{\partial \vec{H}(\vec{r},t)}{\partial t} \tag{3.7}$$

E is the electric field vector; H is the magnetic field vector.

$$\nabla \times \vec{H}(\vec{r}, t) = \epsilon(\vec{r})\epsilon_0 \frac{\partial \vec{E}(\vec{r},t)}{\partial t} + \vec{J}(\vec{r}, t) \tag{3.8}$$

Where ϵ_0 is the permeability of free space, $\epsilon(\vec{r})$ describes the spatial profile of the simulated structure, and $\vec{J}(\vec{r}, t)$ represents the current density vector, which describes the force term or source injected into the problem domain. See Appendix D for the derivation of the wave equation that governs the propagation of electromagnetic waves. The variables of interest in FDTD simulations are the electric field vector and the magnetic field vector.

3.2.2 Discretization and Time Stepping

FDTD method discretizes both space and time into a grid, allowing for the numerical computation of field values at discrete points. This grid-based approach involves iteratively updating the electric and magnetic fields using finite difference approximations of Maxwell's equations. The spatial domain is chosen to ensure that the grid resolution is sufficiently fine to capture the smallest structures within the simulation domain. Each time step updates the electric field components based on the magnetic field components from the previous step, and vice versa [21,22]. This alternating update scheme maintains accurate wave propagation and field interactions within the simulation. An important aspect of FDTD is the relationship between the time step and spatial discretization, which is related to the distance that light can travel in a single time step. This relationship is critical for ensuring the accuracy of the simulation, and it will be discussed in detail in Section 3.2.3 in the context of the Courant–Friedrichs–Lewy (CFL) condition. Essentially, the time step must be sufficiently small to accurately capture the finest spatial steps.

The advantages and limitations of FDTD are quite evident. Because Maxwell's coupled equations are solved directly, FDTD can effectively handle back reflections, index discontinuities, and wide-angle diffraction without issues. However, the computational cost can be substantial. Simulating complex and detailed domains often requires millions of spatial grid points and hundreds of thousands of time steps,

leading to significant memory usage, computational demands, and data storage requirements. For example, the FDTD simulations performed in this study required segmentation of the structure into 50 μm long sections while BPM could model entire structures, albeit based on software from different sources.

3.2.3 Computational Complexity and the CFL Condition

FDTD simulations are computationally demanding due to the requirement for a fine spatial grid and numerous time steps. The Courant–Friedrichs–Lewy (CFL) condition is a critical stability criterion for these simulations [22]. It is expressed as:

$$\frac{c\Delta t}{\Delta x} \leq \mathrm{CLF}_{\max} \tag{3.9}$$

where c is the speed of light in the medium, Δt is the time step, Δx is the spatial grid size, and $\mathrm{CLF}_{\max}$ is a constant less than 1. This condition ensures numerical stability and accuracy, preventing artifacts in the simulation results.

3.3 Summary

Both BPM and FDTD offer valuable tools for simulating optical wave propagation. BPM is effective for rapid, high-quality approximations of guided modes but is limited by its paraxial approximation and inability to handle complex boundary conditions. FDTD, while more computationally demanding, provides a comprehensive analysis of time-dependent electromagnetic wave behavior and can model a wider range of phenomena. Understanding the strengths and limitations of each method is crucial for selecting the appropriate approach based on the specific requirements of a simulation. A full comparison between the two simulation methods is seen in table 1 that highlights the working equation, the key assumptions made, and a computation requirement for a device that is on the order of 500 μm like the LEAC sensor.

Table 3.1: Comparison of Beam Propagation Method (BPM) and Finite-Difference Time-Domain (FDTD) Simulation Techniques: Key Characteristics and Computational Demands

Category	BPM	FDTD
Software	Synopsis RSoft (Will find version)	Tidy3D – version 2.7.1

Fundamental Equations	Helmholtz Equation: $\nabla^2\psi + k_0^2 n^2(x,y,z)\psi = 0$	Maxwell's Equations: $\nabla \times \vec{E}(\vec{r},t) = -\mu_0 \frac{\partial \vec{H}(\vec{r},t)}{\partial t}$ $\nabla \times \vec{H}(\vec{r},t) = \epsilon(\vec{r})\epsilon_0 \frac{\partial \vec{E}(\vec{r},t)}{\partial t} + \vec{J}(\vec{r},t)$
Primary Working Equation	Paraxial wave equation: $\frac{du}{dz} = \frac{i}{2\beta}\left[\frac{d^2u}{dx^2} + \frac{d^2u}{dy^2} + (k^2 - \beta^2)\right]$	Maxwell's Equations $\nabla \times \vec{E}(\vec{r},t) = -\mu_0 \frac{\partial \vec{H}(\vec{r},t)}{\partial t}$ $\nabla \times \vec{H}(\vec{r},t) = \epsilon(\vec{r})\epsilon_0 \frac{\partial \vec{E}(\vec{r},t)}{\partial t} + \vec{J}(\vec{r},t)$
Assumptions	Assumes slow variation in the propagation direction (paraxial approximation).	No inherent assumptions about the nature of the fields or structures.
Computational Demands	Typically, less computationally intensive. Especially when paired with other assumptions such as "Semi-vectorial"	Higher computation requirements then BPM but heavily dependent on the device structure. Both spatial and temporal steps are considered, greatly increasing the computation time.
Key Pros	Fast for simple, large-scale simulations. Easier to implement for waveguides and fiber optics.	Accurate for complex, small-scale, and rapidly varying structures. Can simulate a wide range of physical phenomena without approximations.
Key Cons	Limited to paraxial approximation, making it less accurate for structures with significant variations.	Computationally expensive and requires careful meshing and time-stepping to avoid numerical dispersion.

In summary, while BPM offers a rapid and effective means for conducting tolerance analysis of the LEAC biosensing system, its limitations in handling complex boundary conditions necessitate the use of FDTD for more detailed simulations. Chapter 3 will delve into the tolerance analysis of the LEAC biosensor using BPM simulations, focusing on the dependence of sensitivity on layer thickness. In contrast, Chapter 4 will explore the full device simulation, including multiple sensing regions, using FDTD to accurately model back reflections and complex interactions within the device

CHAPTER 4 – TOLERANCE ANALYSIS

4.1 Previous Work

Much of the work presented in this chapter has been published as a conference manuscript in the 2024 SPIE conference proceedings [23]. In preceding iterations of LEAC biosensor designs, the operational wavelength was fixed at 660 nm. Illustrated in Figure 4.1 is a cross-sectional depiction providing an overview of the device structure. This configuration incorporated a custom-made, 10-micron-thick Silicon-On-Insulator (SOI) silicon detector, situated 1000 nm away from a 30 nm nitride core by an intervening layer of silicon oxide. The nanoscale dimensions of the waveguide core in the vertical dimension resulted in a weakly confined mode, fostering strong interaction with the photodetector through evanescent tail coupling.

The refractive index of the detection region (upper cladding) played a pivotal role in influencing modal coupling. For the sensing region, the upper cladding was deliberately left exposed, facilitating the deposition of a bulk sample of analytes. To measure the generated current, aluminum/titanium contacts were strategically deposited, partially overlapping with the photodetector. These metal contacts were applied to create a continuous 1D array containing both sampling and reference regions.

This multifaceted design allowed for precise control and measurement of the evanescent coupling, making it a novel platform for biosensing applications. The subsequent sections delve into advancements and modifications made to this initial structure, leading to the evolution of the current biosensor design.

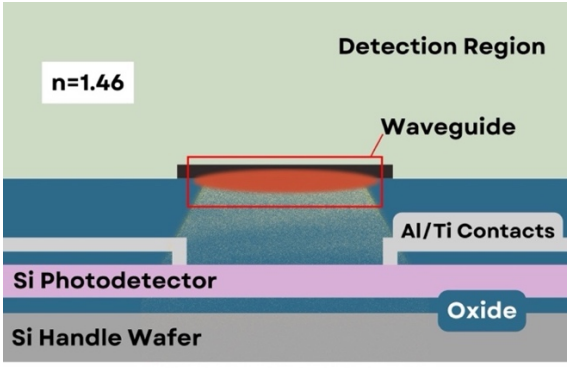

Figure 4.1: LEAC Biosensor Design with 10 µm thick Si photodetector and bulk detection region as described in Reference [3]

4.1.1 Index Sensing Experiment

Previous demonstrations of the device showcased its adaptability with functionalized sensing layers, catering to both biomedical diagnostic [2] and environmental applications [24]. Confirmatory experiments were conducted to validate theoretical predictions. These experiments affirm that an increase in the upper cladding index results in diminished coupling to the photodetector, consequently leading to a reduction in photocurrent. Results validated not only theoretical predictions but also provided crucial insights into the relationship between the upper cladding index and photodetector coupling. The observed decrease in photocurrent aligns with the anticipated behavior, further supporting the functionality of the biosensor design. These earlier works, utilizing the detector specifications, laid the groundwork for understanding the intricate interplay between design parameters and sensor performance. These foundational insights serve as a cornerstone for the advancements and modifications introduced in the current study.

Importantly, the present research places a strong emphasis on the scalability and practicality of the biosensor. By prioritizing mass production through standard fabrication processes, the study aims to optimize the biosensor for widespread application, ensuring its viability in real-world scenarios.

4.2 Simulation parameters

In the pursuit of a comprehensive understanding of the biosensor's robustness under varying fabrication conditions, key parameters were subjected to deliberate variations. The nominal values for the core thickness (t_{core}), lower cladding thickness (t_{clad}), and photodetector layer thicknesses (t_{PD}) were set at 125 nm, 1500 nm, and sub-micron, respectively. These values served as the baseline for subsequent tolerance analyses. A detailed cross-section of the simulated structure is depicted in Figure 4.2, accompanied by corresponding simulation parameters for the index of refraction and absorption of the germanium photodetector.

The variations in core thickness, lower cladding, and detector layer thicknesses allowed for a systematic exploration of the biosensor's response to changes in these critical dimensions. A thin layer of silicon (SOI) was included under the germanium. Both the silicon and germanium are relatively high refractive index, and significantly higher index than the effective index constant of the propagating mode.

Thus, the thickness of the silicon on insulator will have an impact on the relationship between sensitivity and photodetector thickness.

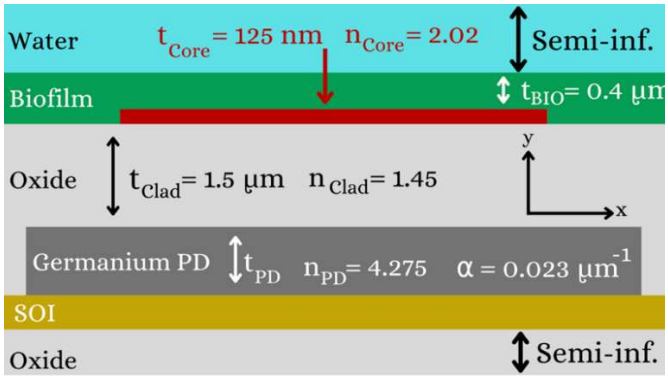

Figure 4.2: Simulated structure cross section with corresponding simulation parameters and detector on SOI

Simulations focused on assessing the power absorbed by a 400 μm long germanium (Ge) photodetector (PD) intricately coupled to a thin Si_3N_4 core through a substantial SiO2 lower cladding. Illustrated in Figure 3 is a cross-section of the simulated structure, where the PD spans y = 0-0.4 μm, the cladding spans y = 0.4-1.9 μm, the core spans y = 1.9-2.0 μm, and the variable refractive index (n = 1.45-1.47) biofilm or sensing region spans y = 2.0-2.4 μm. To capture the nuances of the biosensor's behavior, the equilibrium launch mode was determined using a finite element method, with a non-uniform 10 nm mesh. The effective index of the transverse electric (TE) mode at λ = 1.55 μm was determined without the PD's influence, for example in the z < 100 μm launch region in Figure 3. Silicon on insulator was used below the germanium.

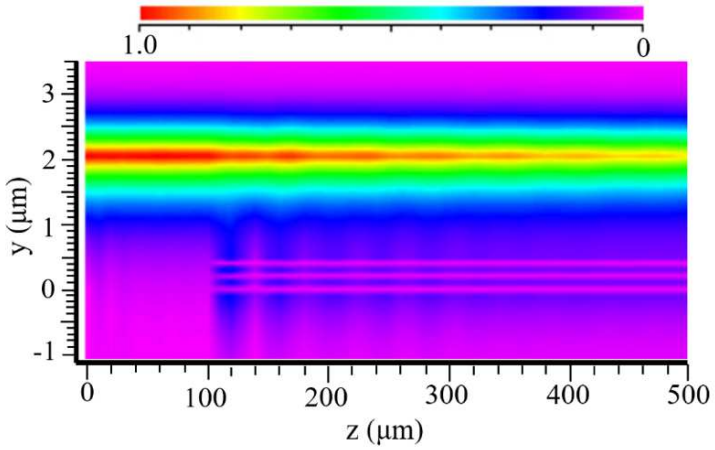

Figure 4.3: Side view of E-field profile of waveguide only (z < 100 μm) and coupling to Ge detector (z > 100 μm) from BPM simulation. The vertical extent of the Ge photodetector spans 0 < y < 0.4 μm while the core spans 1.9 < y < 2.025 μm. Well-defined nodes for the E-field in the photodetector appear as three purple stripes at approximately y = 0 μm, 0.2

μm, and 0.4 μm and indicate a significant lateral standing wave ratio in the photodetector associated with a resonance phenomenon discussed in Section 4.5.

4.3 Device Sensitivity

Absorbed power, which was assumed to correspond to generated photocurrent, forms the foundation for quantifying the biosensor's sensitivity, a crucial aspect in evaluating its efficiency. As the biofilm refractive index (n_{bio}) increases, the generated photocurrent is anticipated to decrease [2]. In this quantitative analysis, the photodetector's absorbed power is directly used to calculate the average absorption coefficient (α_{ave}). This coefficient, in turn, served as a parameter for assessing the device's efficacy in capturing incident light and converting it into photocurrent.

The sensitivity of the biosensor is inherently dependent on the refractive index of the upper cladding (n_{bio}), and it is expressed by the following relationships:

$$\Delta n_{bio} = n_2 - n_1 \tag{4.1}$$

$$\alpha_{ave} = \frac{\alpha_{n2}+\alpha_{n1}}{2} \tag{4.2}$$

$$\Delta\alpha = \alpha_{n2} - \alpha_{n1} \tag{4.3}$$

Finally, normalized sensitivity is derived as:

$$\text{Sensitivity} \equiv \frac{1}{\alpha}\frac{d\alpha}{dn} = \frac{1}{\alpha_{ave}} * \frac{\Delta\alpha}{\Delta n_{bio}}$$

Normalization of sensitivity is implemented to depict a fractional alteration in photocurrent, yielding a dimensionless metric unaffected by the device's physical dimensions or the launch power in the simulation. Heightened sensitivity values correlate with more substantial fractional changes in photocurrent for a given variation in the upper-cladding index.

4.4 Tolerance Analysis

The tolerance analysis for the biosensor involved a systematic exploration of three key parameters critical to its performance. First, the waveguide core thickness was examined, considering the impact of a thinner core on light confinement. Second, variations in lower cladding thickness were investigated, with larger thicknesses affecting evanescent coupling to the photodetector and absolute absorption. Third, the

photodetector thickness was varied, acknowledging that a thicker photodetector could enhance absorption up to a certain point, determined by the penetration depth of the material. Additionally, the device's performance was simulated for both a bulk biological sample and then repeated for a monolayer. This comprehensive analysis facilitated the identification of parameters that yielded stable sensitivity, ensuring a robust and consistent biosensor functionality across diverse conditions. The outcomes of this tolerance analysis provide valuable insights for the design of a biosensor with enhanced reliability.

4.4.1 Validity of results

The validity of the results is underscored by consistent trends observed throughout the simulations. Figure 4.4 illustrates the relationship between absorption and the upper-cladding index in the simulated device.

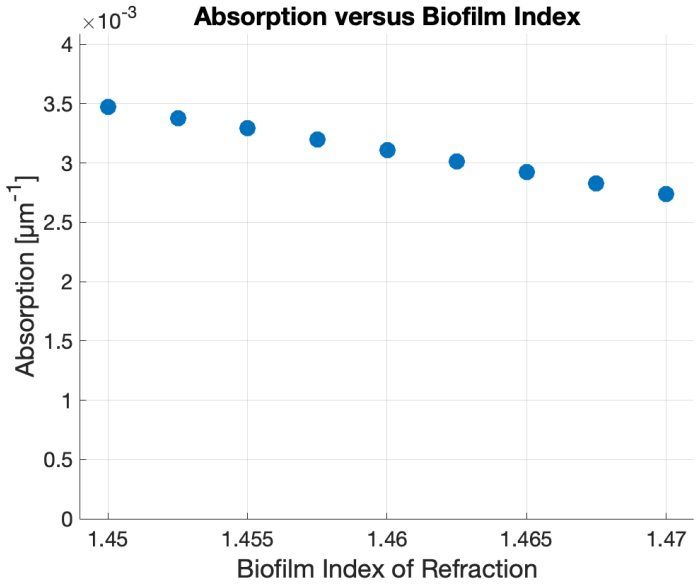

Figure 4.4: Photodetector absorption versus upper cladding index of refraction aligning with previously confirmed theory.

Notably, an increase in the upper cladding index consistently led to a reduction in absorption into the photodetector. Trends align with the established understanding that an increase in refractive index results in decreased coupling, leading to a subsequent decrease in photocurrent. This relationship was consistently observed in simulations, using α as a reliable proxy for photocurrent. Moreover, it is essential to highlight a key distinction between the parameters employed in this simulation and those used in the experimental testing of the biosensor. Consistency in observed trends across simulations reinforces the robustness and

reliability of the results, enhancing the credibility of the study's conclusions. Because the slope of the data in Figure 4.4 is negative, the absolute value of sensitivities is presented below. A larger number represents a more sensitive configuration.

4.4.2 Core waveguide and cladding thickness

The biosensor's sensitivity to core waveguide thickness is detailed in Table 4.1. This analysis is replicated across a specific range of lower cladding thicknesses and upper cladding thicknesses reflecting approximate manufacturing tolerances. The table serves as a comprehensive reference at extreme thicknesses, providing insights into how variations in core waveguide and cladding dimensions impact the biosensor's sensitivity.

Broadening the scope of this analysis to include thin biofilms was imperative. Examining the biosensor's behavior in the presence of nanoscale-bound biological samples becomes pivotal. The investigation into thin biofilm layers runs concurrently, providing valuable insights into how the biosensor performs in conditions pertinent to the detection of minute biological entities.

Table 4.2: Normalized Sensitivity comparison for change in core thickness and lower cladding thickness

$\frac{-1}{\alpha} * \frac{d\alpha}{dn}$	Normalized Absorption: 400 nm Biofilm		
	$t_{Clad} = 1.35$ µm	$t_{Clad} = 1.5$ µm	$t_{Clad} = 1.65$ µm
$t_{core} = 112.5$ nm	24.56	30.15	36.06
$t_{core} = 125$ nm	23.93	27.38	30.11
$t_{core} = 137.5$ nm	20.31	22.03	23.68
$\frac{-1}{\alpha} * \frac{d\alpha}{dn}$	Normalized Absorption: 10 nm Biofilm		
	$t_{Clad} = 1.35$ µm	$t_{Clad} = 1.5$ µm	$t_{Clad} = 1.65$ µm
$t_{core} = 112.5$ nm	0.68	1.01	1.22
$t_{core} = 125$ nm	0.54	0.75	0.87
$t_{core} = 137.5$ nm	0.48	0.65	0.72

The data presented in Table 1 highlights a noteworthy observation: with a lower cladding thickness of 1.5 µm, a smaller core waveguide thickness exhibited the highest sensitivity. This aligns seamlessly with previous research findings [3], reinforcing the notion that a smaller waveguide thickness tends to yield

greater sensitivity, a trend consistently observed in prior experimental data. It's noteworthy that the absorption coefficient conforms to expectations, decreasing with an increase in the refractive index of the sensing region, a pattern corroborated by previous simulations. The normalized sensitivity of the absorption coefficient to changes in refractive index, as displayed in Table 4.1, serves as a non-dimensional measure of performance, providing a metric independent of detector length. The sensitivity's dependence on core and cladding thickness is systematically tabulated for extreme values of variation, incorporating a 10% tolerance around a nominal thickness. Figure 4.5 supplements this information by illustrating intermediate deviations from the nominal layer thicknesses. Specifically, it plots sensitivity as a function of lower cladding thickness for variations in the thickness. Results are compared for both bulk and thin film upper biofilm layers, offering a comprehensive understanding of the biosensor's performance under various structural configurations. Recalling that a thinner waveguide core yields higher sensitivity, the top line in the range of core thickness corresponds to the 112.5 nm core, while the bottom line indicates the 137.5 nm core. This is true for the bulk and thin film simulations.

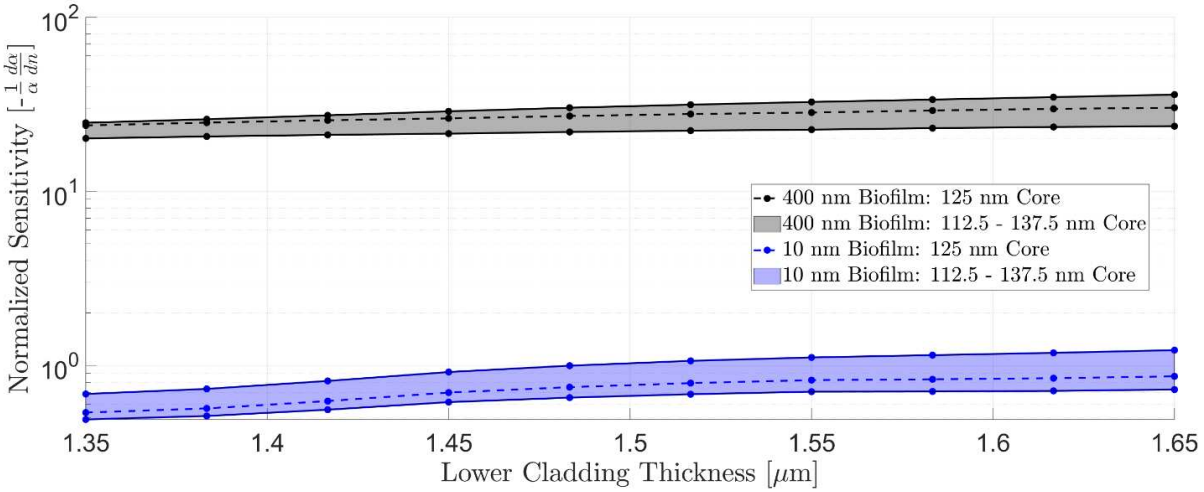

Figure 4.5: Normalized sensitivity versus lower cladding thickness over a 10% manufacturing tolerance with three core thicknesses.

4.4.3 Photodetector thickness

Photodetector thickness is the third key dimension that is susceptible to variation in the manufacturing process. Figure 4.6 provides a visual representation of crucial insights into the absorption characteristics of leaky mode detectors, unveiling a previously unexplored dimension—resonance

phenomena. In contrast to ring resonators and other resonant sensors, prior work on LEAC sensors had assumed they did not display resonant phenomena, broadening their useable refractive index range. However, this study shows that resonances with detector thickness can affect LEAC sensor performance. The insets in the figure display mode profiles and their longitudinal variation relative to the photodetector thickness, offering a comprehensive view of the interplay between absorption and detector thickness. Notably, distinctive peaks emerge, underscoring the existence of resonance at specific thicknesses. This resonance was not observed at the conventional wavelength λ = 660 nm with silicon detectors, presumably because the absorption depth of silicon at that wavelength was substantially shorter than the silicon detector thickness which is not the case for the submicron germanium detectors used here.

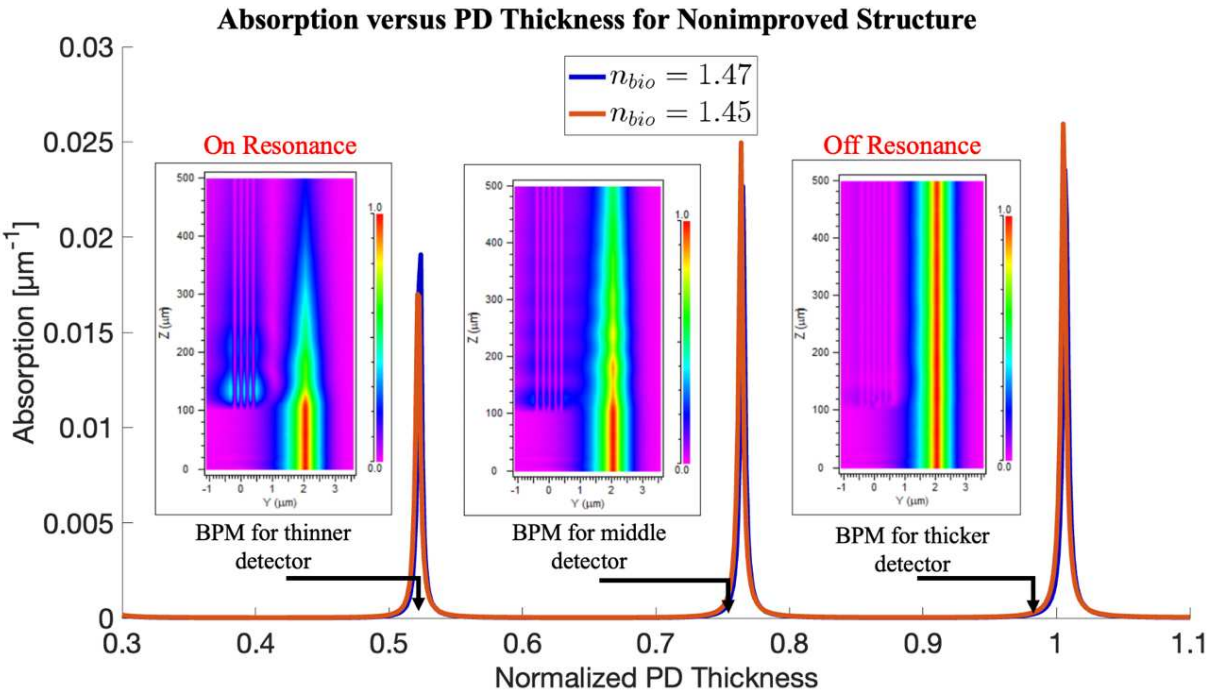

Figure 4.6: Absorption versus photodetector resonance showing inlays of BPM simulations with their mode profiles and their longitudinal variation visible.

These resonant peaks denote regions where the interaction between the core and photodetector reaches an optimum, resulting in increased absorption. However, this newfound avenue presents a formidable challenge in the form of impractically tight tolerances on the photodetector thickness. Recognizing this trade-off, a deliberate approach was considered to shift the location of the resonances away from the desired PD thickness to create a flat sensitivity region within a given tolerance window, these findings underscore

the nuanced interplay between resonance and practical considerations in biosensor design, revealing the need for a balanced approach that considers both sensitivity enhancements and the feasibility of fabrication processes.

4.5 Photodetector Resonance

4.5.1 Sensitivity and improvement

The resonance phenomenon within the biosensor structure manifests in the interaction between the core waveguide and the photodetector, intricately linked to the thickness of the photodetector. This resonance occurrence significantly influences sensitivity, which can be adjusted depending on the proximity of the PD thickness to a resonance peak. A strategic enhancement to the structure involves optimizing the photodetector thickness, ensuring that the sensitivity versus photodetector thickness curve remains flat within a range corresponding to manufacturing tolerance. This optimization approach has been explored for both thin and bulk biofilm layers.

A notable advantage emerges, particularly in the case of bulk biological samples. Sensitivity comparisons between a nominal device and an improved device are illustrated in Figure 4.7. It is crucial to emphasize that the improvement overlay signifies a shift to a different location on the plot. This strategic adjustment in photodetector thickness not only flattens sensitivity but also provides a practical solution that accommodates manufacturing tolerances, showcasing its applicability across different biofilm layer scenarios.

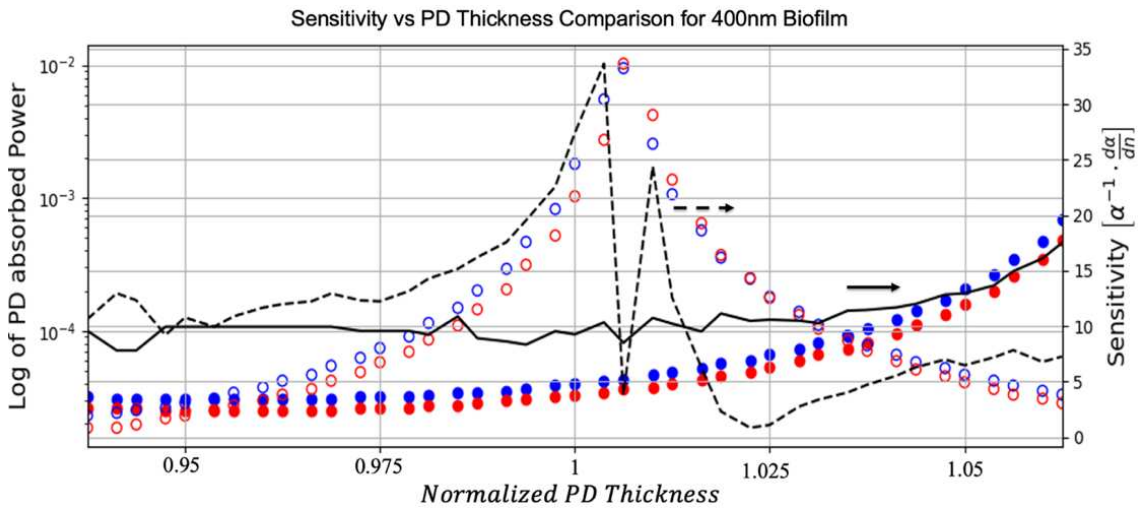

Figure 4.7: Absorption versus sensitivity for a bulk biological sample with the improved structure overlayed. Open (baseline) and filled (improved) circles denote absorbed power read on the lefthand axis. Red circles indicate a biofilm index of 1.45, and blue circles are for a biofilm index of 1.47. The dashed (baseline) and solid (improved) lines show normalized sensitivity read on the righthand axis.

The improvement is evident in Figure 4.7, showcasing a range of photodetector thicknesses that exhibit less sensitivity to variations, particularly when contrasted with the baseline device. While the magnitude of the sensitivity decreases with the improved structure, the goal of this study is to produce a robust and manufacturable. The same comparative analysis for a thinner 10 nm biological sample is presented in Figure 8, where sensitivity is plotted for both the baseline and improved structures.

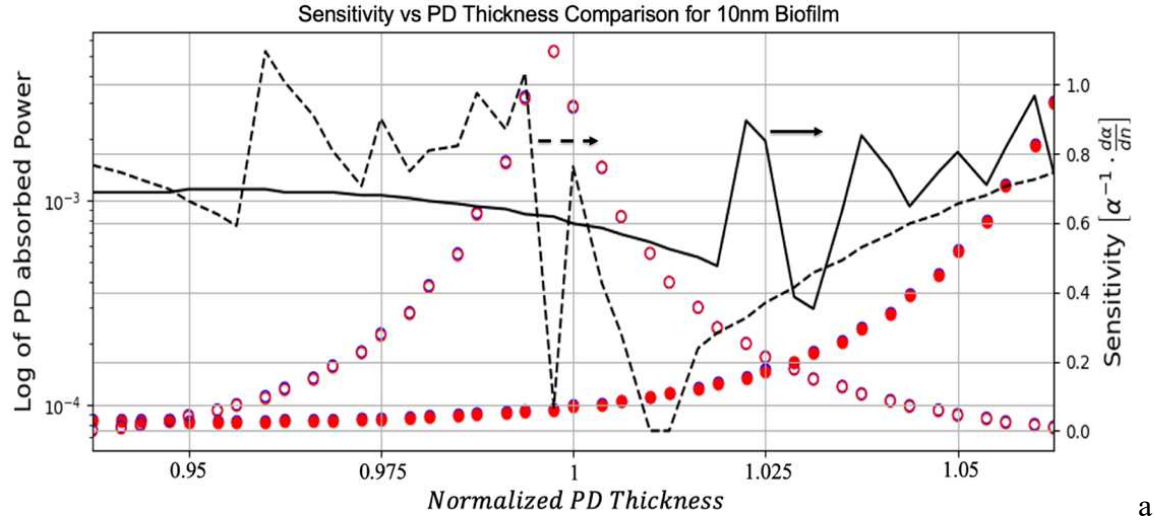

a

Figure 4.8: Absorption versus sensitivity for a thin biological sample with the improved structure overlayed. Symbol keys are the same as in Figure 7.

As anticipated, thin biological samples exhibit a decrease in sensitivity, an expected consequence of the reduced overlap between the bound mode and the biofilm in the upper cladding. Shifting the resonance location also has the same impact in the thin film sample as with the bulk sample. A noteworthy achievement is the maintenance of a flatter sensitivity curve across a range of photodetector thicknesses. This accomplishment aligns with the primary design objective of this study—enhancing manufacturing tolerances.

4.6 Conclusion

Our study delved into the layer thickness tolerances of Local Evanescent Array Coupled (LEAC) biosensors in silicon photonics, with a specific focus on core waveguide, lower cladding, and photodetector thickness variations. Utilizing Beam Propagation Method (BPM) simulations, we found that sensitivity is positively correlated with lower cladding thickness and inversely related to core thickness. The resonance phenomena observed at a long wavelength process with submicron germanium photodetectors presented an innovative opportunity to enhance sensitivity through resonant peaks.

To address manufacturing challenges, we developed an improved biosensor structure that enhanced tolerance to variations in germanium photodiode layer thickness. Our investigation into the biosensor's behavior with bulk and thin biofilm layers revealed that while bulk biofilm layers exhibited promising results and improved sensitivity with the optimized structure, thin biofilm layers posed challenges with lower sensitivity. This underscores the importance of considering practical applications, especially in scenarios involving nanoscale-bound biological samples.

Emphasizing the intricate interplay between design parameters, resonance phenomena, and sensitivity enhancements, this study contributes valuable insights into the adaptability and practicality of LEAC biosensors across diverse scenarios. Our findings successfully bridge theoretical advancements with practical feasibility considerations.

CHAPTER 5 - FULL DEVICE ANALYSIS

To grasp the full concept of the LEAC device, it's essential to begin with an explanation of its overall structure. Earlier discussions have primarily centered around a single sensing region; however, the complete device features an array of sensing regions where multiple sampling events occur. Light traveling from one sampling region to a reference region and then to subsequent sampling regions, raises possible concern of crosstalk. Crosstalk refers to the impact of optical absorption and thus photocurrent in one sensing region on those quantities in subsequent regions or in prior regions due to back reflection. In simpler terms, it investigates the relationship between the flux entering the photodetector in region i_n and the flux in region $i_{n\pm1}$. To thoroughly analyze the full device, both Beam Propagation Method (BPM) and Finite-Difference Time-Domain (FDTD) simulations were employed to simulate a configuration with three detection regions.

5.1 Full Device Structure

FDTD simulations serve two primary purposes: first, to validate BPM results, and second, to identify potential crosstalk within the device. As discussed in Chapter 3, a significant challenge associated with the BPM algorithm is its inability to handle scattering at extreme angles and back reflections as typically implemented. Back reflections from changes in sensing region refractive index or optional segmented photodetectors are likely the primary factor contributing to crosstalk within the device. Figure 5.1 illustrates a continuous photodetector (PD) that spans the entire length of the two sensing regions and intervening reference region without interruption. Each region is 150 μm in length, resulting in a total device length of 450 μm, slightly less than a suggested limit on Ge photodetector length of 500 μm provided by Nick Fahrenkopf of AIM Photonics.

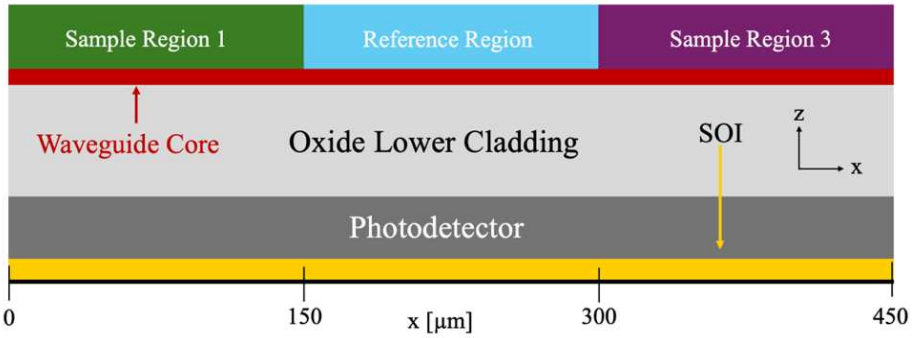

Figure 5.1: Full LEAC device xz cross section with a continuous PD and a 400 nm thick (bulk) biological sample above the waveguide core. Each sample/reference region spans 150 μm. The first region spanning from 0<x<150 μm, the second spanning from 150 ≤x<300, and the third spanning from 300≤x<450

A second configuration is depicted in Figure 5.2, where a segmented photodetector (PD) includes 25 μm breaks at the beginning of each sensing/reference region. Consequently, the full device comprises three 150 μm sample regions and two 25 μm breaks, one between region 1 and the reference region, and another between the reference region and sample region 3. This results in a total device length of 500 μm.

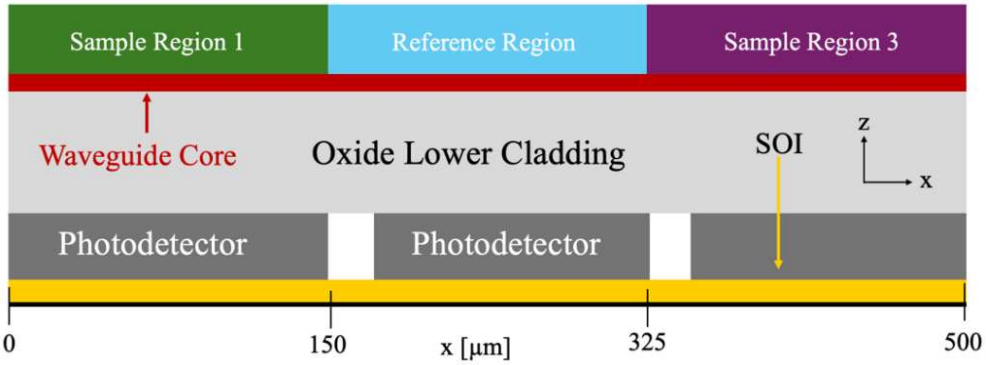

Figure 5.2: Full LEAC device xz cross section with a segmented Pd and a bulk 400 nm thick sample. Each region of the PD is 150 μm long with 25 μm breaks that overlap with next sample, meaning the sample regions are 175 μm long.

These FDTD simulations validate BPM results and provide insights into crosstalk between sensing regions. Additionally, the analysis considers two sample thicknesses: a bulk 400 nm sample for liquid sample detection and a thin 10 nm bound film representative, for example, of surface protein detection. This distinction impacts light interaction within the device and subsequently influences the results including back reflection.

5.1.1 FDTD Simulation Methodology

Considering both continuous and segmented photodetector configurations, this analysis seeks to confirm BPM results through FDTD simulations and identify any potential crosstalk between sensing regions. The simulation parameters used in the BPM simulations remain consistent with those outlined in Section 3.2. FDTD simulations, performed using Tidy3D, utilize a flux monitor at the PD top surface to determine the generated photocurrent. Figure 5.3 illustrates a cross-section of the device simulation parameters. All dimensions are in microns (μm) unless stated otherwise. The flux is measured as the power dissipated from the nitride core, which spans from $0 < z < 0.125$, followed by the sample region extending from $0.125 < z < 0.525$ (or 0.135 for a 10 nm sample), and semi-infinite water spanning the rest of the simulation domain in the positive z direction. The SOI layer spans from $-2.25 < z < -2$, with the submicron photodetector and lower oxide cladding situated above it. PML boundary conditions were applied, utilizing a precise spatial mesh with at least 10 points through each layer.

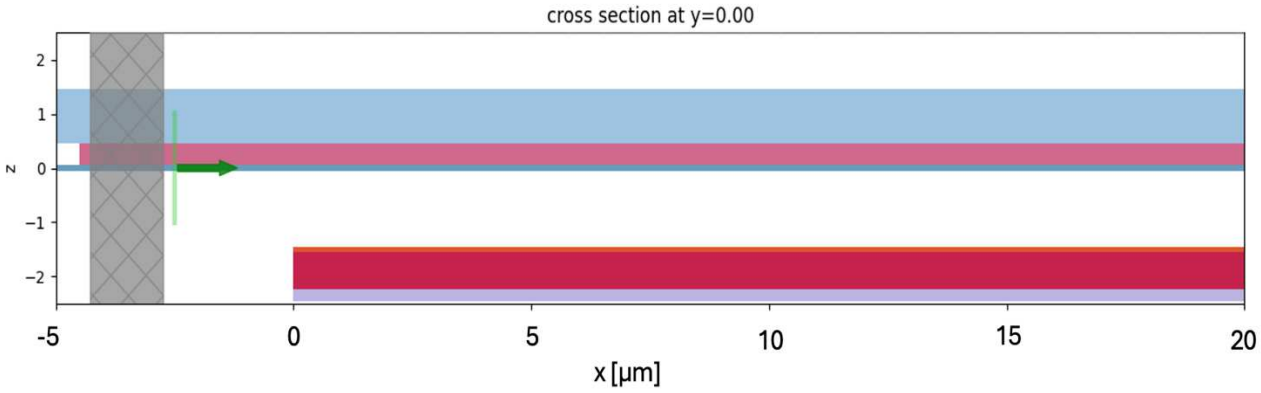

Figure 5.3: xz cross-sectional view of the FDTD simulation domain. The nitride core spans from $0<z<0.125$ followed by the sample region that spans from $0.125<z<0.525$ (or 0.135 for the case of a 10 nm sample) and semi-infinite water spanning the remaining of the simulation domain in the positive z direction. The SOI spans from $-2.25<z<-2$, with the submicron photodetector and lower oxide cladding above it.

Photocurrent in BPM simulations was approximated by examining the total power lost from the waveguide, if 100% of this lost power is converted by the photodetector into photocurrent. Hence, any low angle scattering that exits a problem boundary in BPM simulations would be misinterpreted as photodetector absorption but is assumed negligible. Conversely, the FDTD simulations employed a different metric to quantify relative photocurrent. A flux monitor was included at the boundary of the

photodetector, measuring the total flux across the boundary, normalized against the simulation input power. Flux exiting the bottom boundary of the FDTD simulation beneath a photodetector would be misinterpreted as being absorbed in the photodetector but is assumed to be negligible.

The device was simulated for a range of five refractive indices between 1.45 and 1.47 in both sensing regions, while the reference region was maintained at a constant index of 1.33 (pure water). All combinations of sensing region indices were considered, resulting in 25 possible refractive index combinations between the two sensor regions for the 400 nm sample. Additionally, 10 nm samples were examined with three possible indices of 1.33, 1.44, and 1.55, corresponding to water, a mixture of water and protein, and a protein monolayer, respectively. Nine total combinations were simulated between the first and third sensing regions.

To determine if there is a correlation between two regions, the photocurrent in each detector region at a given index must be normalized against the current in the reference region. In the absence of any normalization, there will clearly be apparent absolute crosstalk as greater absorption (due to smaller sample refractive index) and thus photocurrent in the first sensing region will allow less optical power to reach subsequent sensing regions and thus cause lower photocurrent in the subsequent regions. However, the inclusion of a reference region with a fixed or reference refractive index (pure water in the cases considered here) allows for normalization of the sensing region photocurrent by the reference region photocurrent. The simulation of different combinations of refractive index in the sensing regions allows an exploration of the effectiveness of the normalization against a reference region and the impact of the sensing region being before or after the reference region.

5.2 Full Device BPM and FDTD Simulations Results

In this section, we analyze the results of the full LEAC device across different sample thicknesses—400 nm and 10 nm—for both BPM and FDTD simulations to assess the presence of crosstalk. The challenges with BPM, particularly its limitations in handling back reflections and scattering as discussed in Chapter 2, motivated the need for validation through FDTD simulations. By examining

the device performance with varying sample thicknesses and simulation types, we aim to identify the presence of crosstalk and determine the relative accuracy and efficacy of each simulation method.

5.2.1 400 nm Biological Sample Results

The ratio of sensing currents to reference current was determined by measuring the flux across the photodetector (PD) in each region. Table 1 summarizes the data collected for a 400 nm biological sample with varying indices, using a continuous photodetector in FDTD simulations. This data was also obtained for a segmented detector and repeated the simulations using BPM. The predicted photocurrent ratios are plotted against the index of the corresponding sensing region. A linear regression fit was performed to determine the device's sensitivity, with the slope of the fit indicating how the photocurrent ratio changes with the refractive index of the sensing region (i.e., upper cladding).

Table 5.1: FDTD 400 nm biological sample with continuous detector normalized flux into each detector region with current rations between the two sample regions and reference region.

Region 1 Index	Region 2 Index	Region 3 Index	PD 1 Section 1	PD 2 Reference	PD 3 Section 3	$\frac{I_{sensor_1}}{I_{ref}}$	$\frac{I_{sensor_3}}{I_{ref}}$
1.45	1.33	1.45	0.0409	0.17690	0.0356	0.23160	0.201
1.45	1.33	1.455	0.0409	0.1769	0.0345	0.23150	0.195
1.45	1.33	1.46	0.0409	0.1770	0.0334	0.23146	0.188
1.45	1.33	1.465	0.0409	0.1771	0.0325	0.23143	0.183
1.45	1.33	1.47	0.0409	0.1771	0.0320	0.23141	0.180
1.455	1.33	1.45	0.0385	0.1785	0.0356	0.21580	0.199
1.455	1.33	1.455	0.0385	0.1784	0.0345	0.21584	0.193
1.455	1.33	1.46	0.0385	0.1785	0.0334	0.21574	0.187
1.455	1.33	1.465	0.0385	0.1786	0.0325	0.21571	0.182
1.455	1.33	1.47	0.0385	0.1786	0.0320	0.21567	0.179
1.46	1.33	1.45	0.0358	0.1802	0.0357	0.19878	0.198
1.46	1.33	1.455	0.0358	0.1802	0.0345	0.19877	0.191
1.46	1.33	1.46	0.0358	0.1802	0.0334	0.19875	0.185
1.46	1.33	1.465	0.0358	0.1802	0.0325	0.19872	0.181
1.46	1.33	1.47	0.0358	0.1803	0.0320	0.19869	0.177
1.465	1.33	1.45	0.0331	0.1823	0.0358	0.18204	0.196
1.465	1.33	1.455	0.0331	0.1823	0.0346	0.18203	0.190
1.465	1.33	1.46	0.0331	0.1823	0.0335	0.18201	0.184
1.465	1.33	1.465	0.0331	0.1823	0.0326	0.18201	0.179
1.465	1.33	1.47	0.0331	0.1823	0.0321	0.18198	0.176
1.47	1.33	1.45	0.0308	0.1842	0.0359	0.16735	0.194
1.47	1.33	1.455	0.0308	0.1842	0.0347	0.16734	0.188
1.47	1.33	1.46	0.0308	0.1842	0.0336	0.16732	0.182
1.47	1.33	1.465	0.0308	0.1842	0.0323	0.16732	0.175
1.47	1.33	1.47	0.0308	0.1842	0.0322	0.16731	0.174

Figure 5.4a shows the BPM simulation data in red and the FDTD simulation data in blue for a continuous detector with a 400 nm sample, while Figure 4.4b presents the same for the segmented detector. The plotted data includes 25 points, representing the sample index of refraction combinations between the first and third regions. The dotted lines indicate the linear regression of the ratio of the photocurrent in the first region to the reference region, while the solid lines represent the regression of the

ratio of the third region to the reference region. This approach is consistent throughout all full device simulations. In the bottom left corner, a zoomed-in section illustrates the spread of the data points in the third detection region. This spread can be thought of as five distinct traces, each corresponding to a different index for the first region.

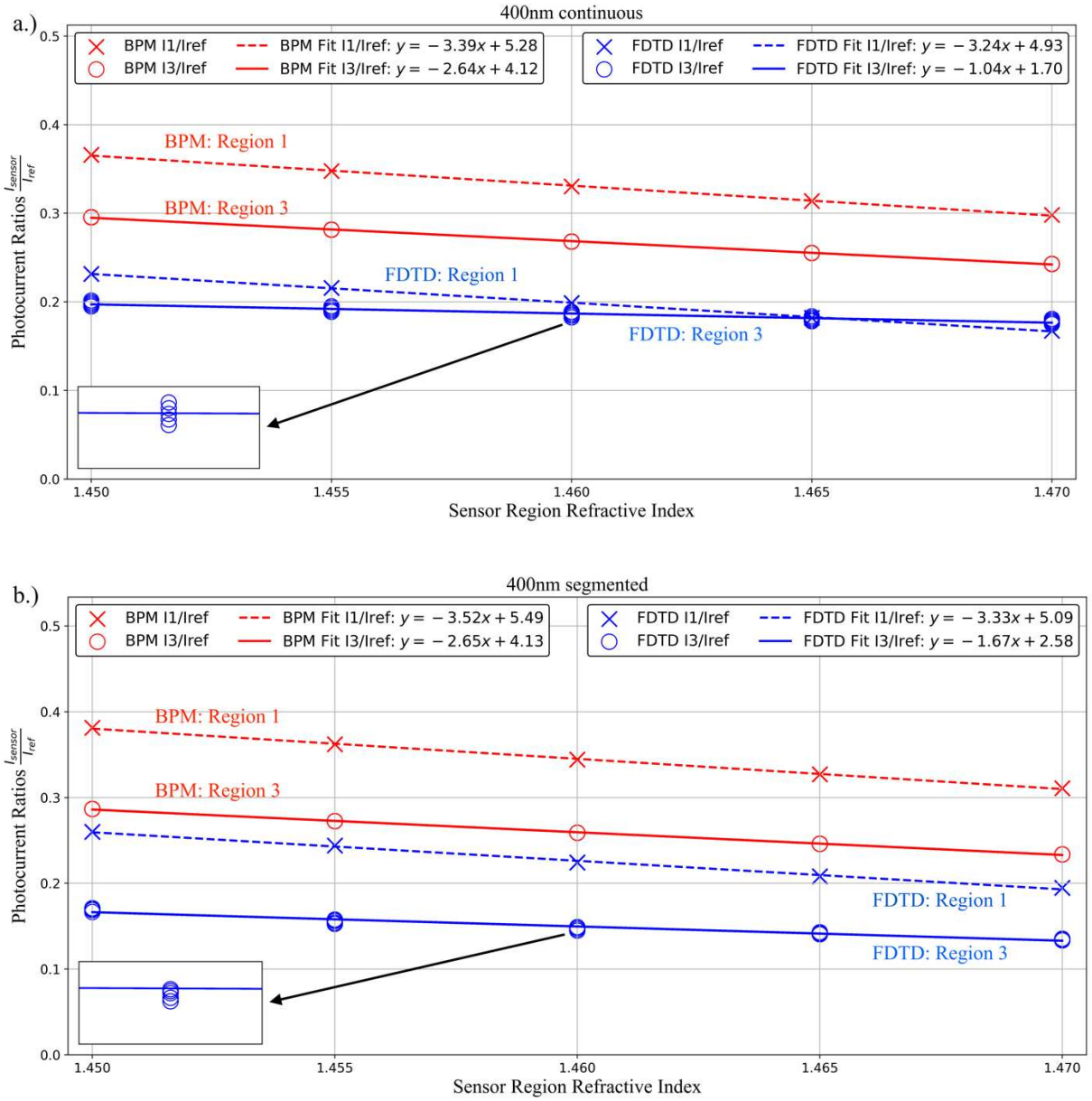

Figure 5.4: Full LEAC device BPM simulations for a bulk 400 nm biological sample with the ration of the sensor region current to the reference region current plotted against in the index of refraction. 5 different indexes were considered, giving 25 combinations between the first and third sensing regions. Linear regressions were fitted for each ratio . a.) Shows a continuous photodetector consistent with figure 5.1. b.) Shows a segmented photodetector consistent with figure 5.2

For each value of sensing region index plotted on the horizontal axis in Figure 5.4, there are five nearly identical photocurrent ratios generated for different values of the sample refractive index in the other region, demonstrating minimal dependence and thus minimal crosstalk induced by the other region. For example, for the blue plus signs, which represent the photocurrent ratio of $I_{sensor3}/I_{ref}$, at a sensor index of $n_3 = 1.47$ on the horizontal axis, the index of the first sensor region varies among $n_1 = 1.450$, 1.455, 1.460, 1.465, and 1.470. Because those five points have such similar photocurrent ratios (0.1807, 0.1792, 0.1778, 0.1764, 0.1749 – an approximately 3% spread), the green blue signs fall indistinguishably on top of each other in the plot.

5.2.3 10 nm Biological Sample Results

Like Section 5.2.2, Table 5.2 summarizes the data collected for a 10 nm biological sample with varying indices, using a continuous and photodetectors in FDTD simulations. This data was also obtained for the segmented detected and by repeated using BPM. The predicted photocurrent ratios are plotted against the index of the corresponding sensing region. A linear regression fit was performed to determine the device's sensitivity, with the slope of the fit indicating how the photocurrent ratio changes with the refractive index of the sensing region (i.e., upper cladding)

Table 5.2: FDTD 10 nm biological sample with continuous detector normalized flux into each detector region with current rations between the two sample regions and reference region.

Region 1 Index	Region 2 Index	Region 3 Index	PD 1 Section 1	PD 2 Reference	PD 3 Section 3	$\frac{I_{sensor_1}}{I_{ref}}$	$\frac{I_{sensor_3}}{I_{ref}}$
1.33	1.33	1.45	0.216	0.1390	0.0927	1.557	0.666
1.33	1.33	1.455	0.216	0.1388	0.0901	1.559	0.649
1.33	1.33	1.46	0.216	0.1386	0.0873	1.561	0.630
1.44	1.33	1.465	0.211	0.1404	0.0936	1.500	0.667
1.44	1.33	1.47	0.211	0.1402	0.0911	1.502	0.649
1.44	1.33	1.45	0.211	0.1401	0.0883	1.503	0.630
1.55	1.33	1.455	0.205	0.1419	0.0947	1.441	0.667
1.55	1.33	1.46	0.205	0.1417	0.0920	1.443	0.649
1.55	1.33	1.465	0.205	0.1416	0.0893	1.444	0.630

Figure 5.5a shows the BPM simulation data in red and the FDTD simulation data in blue for a continuous detector with a 10 nm sample, while Figure 5.5b presents the same for the segmented detector.

The plotted data includes 9 points, representing the sample index of refraction combinations between the first and third regions. The dotted lines indicate the linear regression of the ratio of the photocurrent in the first region to the reference region, while the solid lines represent the regression of the ratio of the third region to the reference region. This approach is consistent throughout all full device simulations. In the bottom left corner, a zoomed-in section illustrates the spread of the data points in the third detection region.

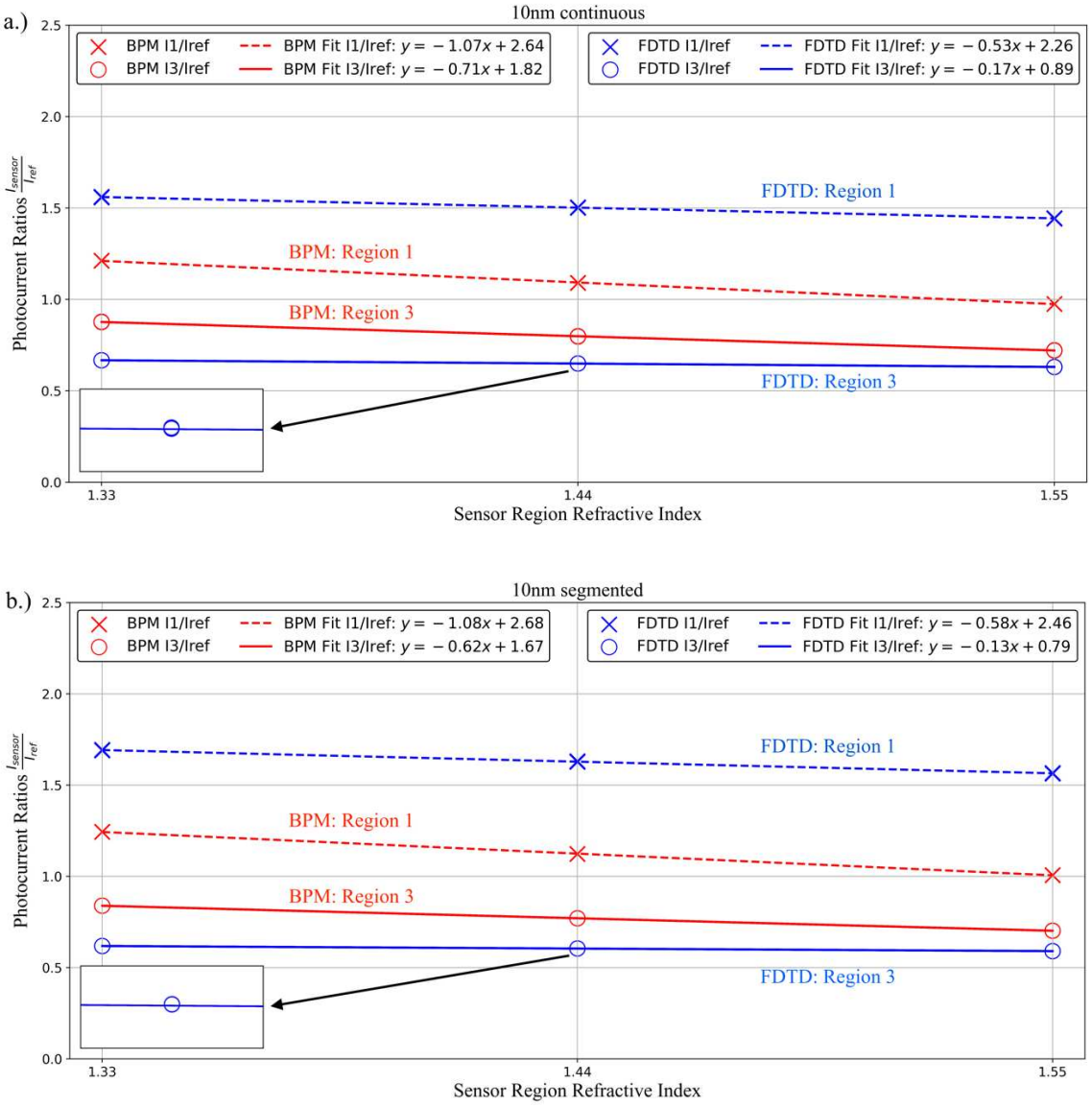

Figure 5.5: Full LEAC device BPM simulations for a bulk 10 nm monolayer sample with the ratio of the sensor region current to the reference region current plotted against in the index of refraction. 3 different indexes were considered, giving 9 combinations between the first and third sensing regions. Linear regressions were fitted for each ratio

The data obtained from both the BPM and FDTD simulations demonstrate consistency across different scenarios. Both simulation methods reveal a clear, monotonic decrease in the generated photocurrent as the refractive index of the upper cladding increases. This trend is consistently observed across varying sample thicknesses and detector types, underscoring the sensitivity of the photocurrent to changes in the refractive index. The tables below (Tables 5.3 and 5.4) provide a direct comparison and summary of the regression slopes derived from these simulations.

Table 5.3: Summary of Regression Slopes for Photocurrent Ratios (400 nm Sample)

Detector Type	Simulation Method	Region 1 Regression Slope	Region 3 Regression Slope
Continuous	BPM	-3.39	-2.64
Continuous	FDTD	-3.24	-1.04
Segmented	BPM	-3.52	-2.65
Segmented	FDTD	-3.33	-1.67

Table 5.4: Summary of Regression Slopes for Photocurrent Ratios (10 nm Sample)

Detector Type	Simulation Method	Region 1 Regression Slope	Region 3 Regression Slope
Continuous	BPM	-1.07	-0.71
Continuous	FDTD	-0.53	-0.17
Segmented	BPM	-1.08	-0.62
Segmented	FDTD	-0.58	-0.13

The comparison between BPM and FDTD simulation data highlights a consistent trend in the behavior of photocurrent as a function of refractive index, with both methods showing similar patterns of decline. The fact that the regression slopes are of the same order suggests that both methods effectively capture the fundamental physics governing the interaction between the waveguide and the photodiode. However, the observed discrepancies in the magnitude of these slopes reveal important differences in the simulation approaches and the assumptions made in the study. Firstly, BPM consistently yields higher slope values, likely due to the assumption that all power lost from the waveguide is coupled directly into the photodiode and converted with 100% efficiency to an electrical signal. This assumption likely contributes to the higher photocurrent estimates observed in the BPM data.

Secondly, we observe an additional discrepancy where the slope for the segmented detector in the FDTD simulations is significantly smaller—approximately half—of that in the BPM simulations. This difference highlights one of the largest drawbacks of BPM: the lack of back reflection, combined with the assumption. In the FDTD simulations, there is a large discontinuity in the mode's effective index at the break of the segmented detector. A significant portion of the mode is guided into the photodetector, and once the break occurs, there is instability in the mode that causes power to be lost from the waveguide but not coupled into the photodetector. This phenomenon, which is more accurately captured by FDTD, underscores the limitations of BPM in scenarios where back reflection and mode stability are critical. This issue will be discussed in more detail in Section 5.3.

These insights emphasize the importance of considering the assumptions and limitations of each method when interpreting simulation results. In practical terms, while BPM can provide a quick and generally accurate estimation of photocurrent trends, FDTD offers a more nuanced and detailed view that better account for complex interactions within the device. Future work could involve refining the BPM model to reduce these discrepancies or further exploring the conditions under which each method is most reliable.

5.2.4 Presence of Crosstalk

In the context of the LEAC biosensor, crosstalk refers to the interaction between sensing regions, where optical absorption or reflections in one region influences the photocurrent detected in preceding or subsequent regions. This effect becomes particularly significant when reflections occur at boundaries between regions with differing refractive indices. Crosstalk can occur in two directions: forward crosstalk, where changes in an earlier sensing region (e.g., region 1) affect the photocurrent in a later region (e.g., region 3), and backward crosstalk, where changes in a later region influence the photocurrent in an earlier region.

To qualitatively observe the presence of crosstalk, we examined the variation (or spread) in the photocurrent ratio data between the first and third sensing regions. A significant spread in this data

indicates a relationship between these regions. Specifically, it suggests that changes in the refractive index of one region affect the photocurrent in the other, whether in the forward or backward direction.

This phenomenon is most clearly illustrated in Figure 5.4a, which presents the results for a 400 nm bulk sample. The increased thickness of the sample amplifies the potential for crosstalk due to greater reflection at the dielectric boundary between the sensing and reference regions. A close examination of Figure 5.4a reveals a spread of points in the solid blue trace, which represents the ratio of photocurrent in region 3 relative to the reference region. Figure 5.6 provides a zoomed-in view of this trace, offering a clearer depiction of the spread and highlighting the presence of forward crosstalk.

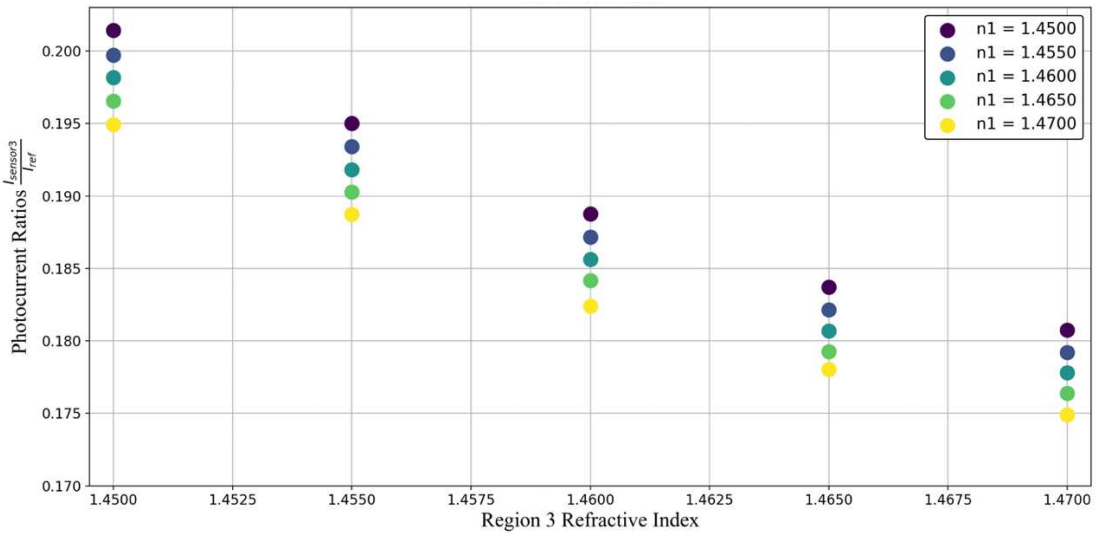

Figure 5.6: Photocurrent ratio in the third sensing region to the reference region for a 400 nm biological sample with a continuous photodetector (PD). Data points are color-coded based on the refractive index of region 1 (n_1), showing how changes in n_1 affect the photocurrent ratio in region 3.

The spread in the data across different refractive index combinations for regions 1 and 3 prompted the decision to apply ANOVA to quantify the presence of crosstalk. It is crucial to differentiate between two types of crosstalk: absolute photocurrent crosstalk, where the photocurrent in one region depends on the refractive index of another region, and photocurrent ratio crosstalk, which considers the ratio of the photocurrent in each region to the reference region. In BPM simulations, forward crosstalk can occur in the absolute photocurrent, as the photocurrent in the third region is reduced by optical absorption in the

earlier regions, and optical absorption in the earlier region is in turn dependent on the refractive index in that region . However, by using photocurrent ratios, this type of forward crosstalk is largely eliminated because the photocurrent in each sensing region is normalized by the reference region between sensing regions, which ensures that variations in total power are accounted for. This is why Figure 5.4a shows minimal spread in the BPM data. The ratio effectively removes the influence of optical power loss as light propagates through the device, ensuring that photocurrent differences are only driven by local changes in the refractive indices of the sensing regions. FDTD simulations, on the other hand, fully solve the electromagnetic fields, including back propagation and other interactions at dielectric boundaries that are not captured by BPM. These additional effects, particularly back reflections, lead to crosstalk that cannot be fully eliminated by using ratios alone. This is evident in Figure 5.6, where the spread in the photocurrent ratios for the 400 nm sample remains, suggesting that normalization does not fully mitigate crosstalk in FDTD simulations. For thinner samples, such as the 10 nm case in Figure 5.7, crosstalk is significantly reduced, as indicated by the smaller spread in the data.

The material simulated above the biofilm, regardless of the biofilm thickness, is uniformly pure water with a refractive index of n = 1.33 for all regions. So, index discontinuities, which are the cause of back reflection, in the upper cladding only occur in the biofilm layer. Consequently, with a thinner biofilm layer, there is less change in the mode's effective index, resulting in reduced reflection.

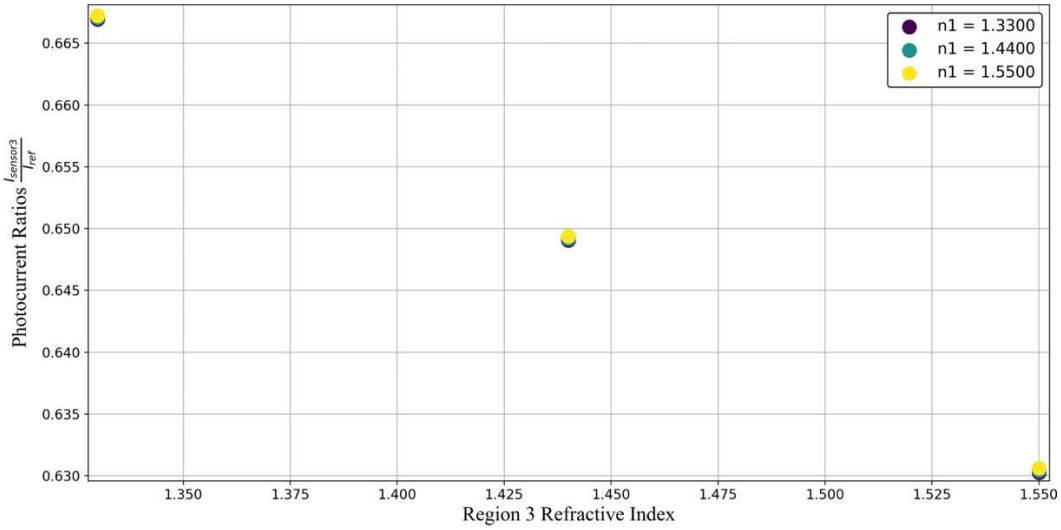

Figure 5.7: Zoomed in plot of the FDTD full device simulation with a 10 nm biological sample for a continuous PD. Here the ratio of the current in the third sensing region over the reference region is plotted.

To quantify the significance of these interactions, ANOVA was applied to determine whether changes in region 1's refractive index have a statistically significant impact on the photocurrent ratio in region 3, and vice versa, whether changes in region 3 affect the photocurrent ratio in region 1. This statistical analysis helps to further dissect how different factors, such as sample thickness and simulation method, contribute to the observed crosstalk in both forward and reverse directions in the full device.

5.2.5 Statistical Analysis of Crosstalk Using ANOVA

ANOVA isolates the effects of n_1 and n_3 on photocurrent ratios in each region, allowing us to dissect forward and reverse crosstalk. This analysis determines whether refractive index changes significantly impact device performance and whether these effects differ across simulation types and sample thicknesses. Data were gathered from simulations with continuous and segmented photodetector configurations for 400 nm and 10 nm samples.

Linear regression models quantified the relationships between n_1, n_3, and the photocurrent ratios in both regions. ANOVA was used to determine the statistical significance of these relationships by comparing p-values to a significance threshold (α=0.05). The interpretation of the null hypothesis varied by region: for the first detector region (I_1/I_{ref}), we expect to reject the null hypothesis for n_1, confirming its significant influence on the photocurrent ratio for region 1. Without reverse crosstalk, we expect to accept the null hypothesis for n_3, indicating that n_3 has minimal influence on the photocurrent in this region. For the third detector region (I_3/I_{ref}) the null hypothesis states that neither n_1 nor n_3 influences the photocurrent. Here, we expect to accept the null hypothesis for n_1 indicating minimal forward crosstalk, and reject it for n_3, confirming its influence.

While ANOVA provided insights into the statistical significance of refractive index changes on photocurrent ratios, it became evident that p-values alone did not fully capture the strength of these relationships. To better understand how strongly the photocurrent ratios depend on refractive index variations, we transitioned to analyzing crosstalk ratios, which quantify the sensitivity and cross-

sensitivity of the device to changes in n_1 and n_3. Crosstalk ratios are defined as the derivatives of the photocurrent ratios with respect to the refractive indices, allowing us to measure how much the current ratios I_1/I_{ref} and I_3/I_{ref} depend on changes in n_1 and n_3. Specifically, the forward crosstalk ratio reflects the sensitivity of I_3/I_{ref} to changes in n_1. This ratio is defined as:

$$C_{forward} = \frac{\frac{d}{dn_1}\left(\frac{I_3}{I_{ref}}\right)}{\frac{d}{dn_3}\left(\frac{I_3}{I_{ref}}\right)}$$

Similarly, the reverse crosstalk ratio measures the impact of n_3 on I_1/I_{ref} and can be defined as:

$$C_{reverse} = \frac{\frac{d}{dn_3}\left(\frac{I_1}{I_{ref}}\right)}{\frac{d}{dn_1}\left(\frac{I_1}{I_{ref}}\right)}$$

Tables 5.5 summarize the forward and reverse crosstalk ratios for both continuous and segmented photodetector configurations, across 400 nm and 10 nm samples

Table 5.5: Forward and reverse crosstalk ratio across different sample thicknesses and detector configurations for current ratios

$C_{forward}$		
Simulation Method	Continuous PD	Segmented PD
400 nm Sample		
BPM	0.0087	0.0018
FDTD	0.3048	0.0013
10 nm Sample		
BPM	0.0111	0.0023
FDTD	0.0073	0.0018
$C_{reverse}$ 400 nm Sample		
BPM	0.0	0.0
FDTD	0.0001	0.0022
10 nm Sample		
BPM	0.0	0.0
FDTD	0.0314	0.0313

The use of photocurrent ratios was prompted by the inclusion of a reference region to account for forward crosstalk. By incorporating a reference break between the first sample region and the third sample region, the photocurrent ratios effectively normalize the data against crosstalk effects. To confirm that this ratio eliminates the crosstalk, we computed the crosstalk ratios using absolute currents generated in each region, rather than the photocurrent ratios with the reference. The forward crosstalk ratio reflects the sensitivity of I_3 to changes in refractive index. This ratio is defined as:

$$\bar{C}_{forward} = \frac{\frac{d}{dn_1}(I_3)}{\frac{d}{dn_3}(I_3)}$$

Similarly, the reverse crosstalk ratio measures the impact of the index on I_1 and can be defined as:

$$\bar{C}_{reverse} = \frac{\frac{d}{dn_3}(I_1)}{\frac{d}{dn_1}(I_1)}$$

The results, presented in Tables 5.6, demonstrate that the photocurrent ratios successfully mitigate crosstalk, as evident when comparing these ratios to the absolute current data. This confirms that the reference region effectively normalizes the data and isolates the signal from forward crosstalk

Table 5.6: Forward and reverse crosstalk ratio across different sample thicknesses and detector configurations for absolute current

Simulation Method	Continuous PD	Segmented PD
400 nm Sample		
BPM	0.0266	0.0283
FDTD	0.001	0.0228
10 nm Sample		
BPM	0.1849	0.2070
FDTD	0.3531	0.4312
400 nm Sample		
BPM	0.0	0.0
FDTD	0.0	0.0
10 nm Sample		
BPM	0.0	0.0
FDTD	0.0	0.0

Tables 5.5 and 5.6 provide a detailed analysis of crosstalk in the full LEAC device. The results are clear: in region 3, photocurrent ratios effectively account for forward crosstalk. The forward crosstalk ratio in region 3 confirms minimal influence from region 1's refractive index, indicating that the photocurrent in region 3 is not affected by changes in n1. However, raw current data in region 3 shows a significantly higher forward crosstalk ratio, indicating a stronger dependence of the photocurrent on region 1's refractive index.

A surprising result appears in the 10 nm FDTD simulations. Photocurrent ratios reveal reverse crosstalk in region 1, with a low reverse crosstalk ratio indicating sensitivity to changes in region 3's refractive index. This effect does not appear when using raw current data. The reason is that the reference current (Iref) depends on region 3's refractive index, introducing this dependence into the analysis for region 1 when using ratios. Photocurrent ratios reduce forward crosstalk in region 3 but introduce a

dependence on region 3's refractive index (via Iref), which is absent when using raw current data. Ratios mitigate forward crosstalk, while raw currents provide a method to counteract reverse crosstalk.

5.2.6 Impact of Crosstalk on Sensitivity

Quantifying the impact of crosstalk on the total sensitivity of the device remains a consideration. From the data in Figures 5.7 and 5.8, sensitivity can be defined as the magnitude of the change in the ratio of photocurrent between the sensing region and the reference region over the change in the refractive index:

$$\text{sensitivty} \equiv \left| \frac{d\left(\frac{I_{sensor}}{I_{ref}}\right)}{dn} \right| \tag{5.1}$$

Where I_{sensor} is the photo current measured in whichever sensing region, I_{ref} is the photocurrent measured in the reference region, and n is the index of refraction of the biological sample. Referring to the linear regression performed on each data set, the slope of this regression represents the sensitivity of the device, as defined in Equation 5.1. The data spread caused by crosstalk introduces uncertainty in the actual sensitivity of the device. This can be interpreted as the percent error in sensitivity, resulting from the variability in the normalized photocurrent as a function of the change in the reference region current:

$$\delta \equiv \frac{\Delta\left(\frac{I_{sensor}}{I_{ref}}\right)}{\left| \frac{d\left(\frac{I_{sensor}}{I_{ref}}\right)}{dn} \right|} * 100 \tag{5.2}$$

Where $\Delta\left(\frac{I_{Sensor}}{I_{ref}}\right)$ is the range of current ratio values for a specific index (i.e. $\max\left(\frac{I_{sensor}}{I_{ref}}(n_i)\right) - \min\left(\frac{I_{sensor}}{I_{ref}}(n_i)\right)$)

Looking at the extreme case of a bulk 400 nm biological sample with a continuous photodetector, the percent error can be quantified using Equation 5.2 as:

$$\delta = \frac{0.1887 - 0.1824}{|-1.05|} * 100 = 0.6\%$$

In the case of a bulk biological sample, a percent error of approximately 1% due to crosstalk can be expected. For the 10 nm biological sample, the percent error is nearly zero, reflecting the low impact of crosstalk. Additionally, this error is not observed in the first sensing region.

5.3 Segmented vs. Continuous Detector Discrepancies

In most cases, the results for the continuous and segmented detectors are similar, if not identical. However, a discrepancy is observed in Figure 5.5a. For the bulk 400 nm biological sample with a continuous detector, the ratio of sensor current to reference current between region 1 and region 3 crosses over, indicating more photocurrent in the third sensing region than in the first. This is counterintuitive due to the exponential decay of the mode's power as it propagates down the waveguide and is absorbed by the photodetector.

The explanation for this discrepancy lies in examining the cross-sectional field monitor for the FDTD simulations in the first 25 μm of the third sensing region. Figure 5.9 shows the x-z cross-section of the FDTD simulation domain, where x is the propagation direction, z is normal to the wafer, and y is the transverse direction. In Figure 5.9a, the photodetector (PD) is continuous for the 30 μm after the device transitions from the reference region to the third sensing region. Figure 5.9b, on the other hand, shows the same 30 μm, with 25 μm of the break between the detectors (note that the 20 μm are shown here for detection, but there are 25 μm in the simulation).

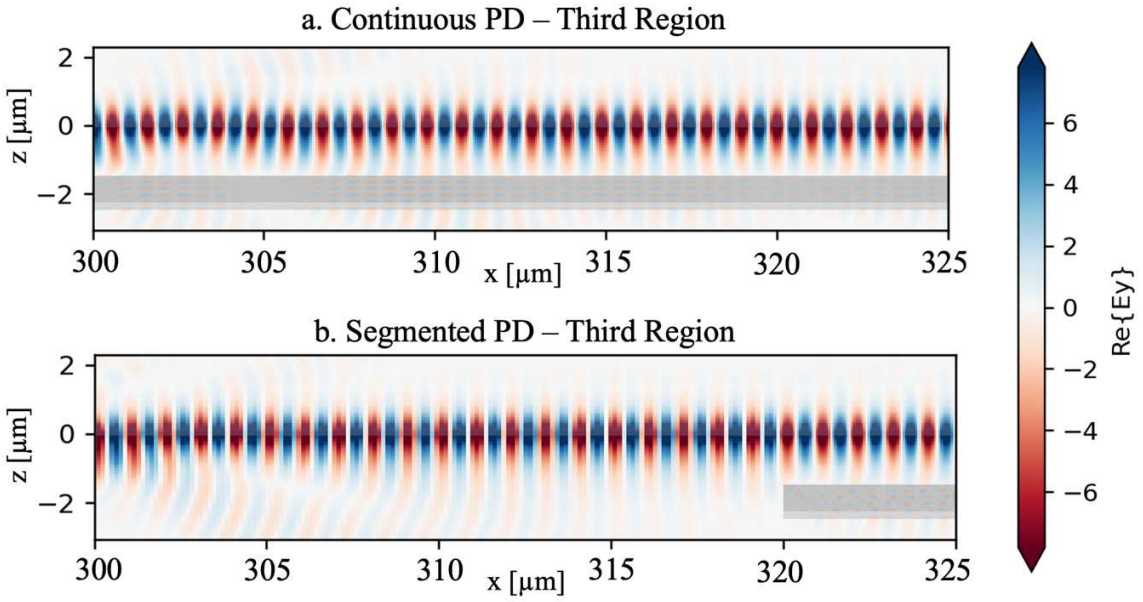

Figure 5.9: xz cross-sectional view of the FDTD full LEAC device field monitor field monitor for the 30 µm following the dielectric interphase between the reference region and third sensing region. a.) The continuous PD shows an increase in flux across the PD due to the instability of the mode. b.) In the segmented detector there is still an increase in flux as the mode stabilizes but the power is lost due to the gap between the photodetector segments.

In both figures the mode becomes unstable following the reference region, due to the abrupt change in the index of refraction in the upper cladding. This abrupt change causes a ringing in the mode as it reconfines. In Figure 5.9a, the beating of the mode causes regions of increased flux into the photodetector. This is not present in Figure 5.9b because the excess flux created as the mode stabilizes occurs before the PD. Increased photocurrent for the continuous PD accounts for the increased generated photocurrent in the third region. This was further confirmed by placing a flux monitor in the 25 µm gap region for the segmented PD. The difference between the flux for the continuous and segmented PD in region three was equal to the flux that occurred in the gap for the segmented PD.

5.4 Conclusion

In this chapter, the full LEAC biosensor device was analyzed using both BPM and FDTD simulations for two detector configurations to assess crosstalk between sensing regions and its impact on device sensitivity. FDTD validated the BPM results while highlighting BPM's inability to capture back reflections and scattering, especially in segmented detectors, where mode instabilities increased crosstalk.

Crosstalk was most prominent in the 400 nm biological sample, contributing to greater uncertainty in sensitivity measurements, whereas it was minimal in the 10 nm sample.

The use of photocurrent ratios successfully accounted for forward crosstalk in region 3, as confirmed by high p-values indicating no significant influence from the first region's refractive index. However, raw current data in region 3 showed a much smaller p-value, suggesting stronger dependence on the first region, indicating the presence of forward crosstalk. Interestingly, in the 10 nm FDTD simulations, photocurrent ratios introduced reverse crosstalk in the first region, which was not observed in the raw current data. This discrepancy is likely due to the reference region current's dependence on the third region's index, which was introduced when using the ratios. Statistical analysis using ANOVA confirmed the presence of both forward and reverse crosstalk for bulk samples, but reverse crosstalk due to reflections at dielectric boundaries remained negligible for all analytes and detectors, particularly when using raw currents.

CHAPTER 6 – COUPLED MODE THEORY

Coupled Mode Theory (CMT) describes the interactions between electromagnetic modes in waveguides and photonic structures. Under ideal conditions with perfect phase matching (when the propagation constants of interacting modes are closely aligned, allowing efficient energy transfer), energy transfer between these modes is simple and periodic. However, in real-world applications, complexities such as material losses, leaky modes, and phase mismatches disrupt this ideal energy exchange, leading to more intricate power distribution patterns along the waveguide [25].

This chapter extends CMT to address these practical challenges. It presents a framework that accurately models the complex power behaviors observed in coupled waveguide-photodetector system simulations, where critical parameters such as photodetector thickness, absorption coefficients, and waveguide properties play significant roles. A primary focus is on phase mismatch between waveguide and photodetector modes: minimizing this mismatch enables resonant coupling and enhanced absorption, while significant mismatches reduce energy transfer. Additionally, material losses, represented by complex loss coefficients, introduce oscillatory power decay as guided modes lose energy over distance. By integrating these factors into the coupled mode equations, we develop a more robust model that describes mode coupling in lossy environments and predicts resonance conditions and critical coupling scenarios.

Ultimately, the complex power fluctuations observed in simulations are not numerical artifacts but real phenomena, explained by this extended CMT framework. This enhanced understanding supports the simulation results and offers deeper insight into the dynamic behavior of real-world photonic systems.

6.1 Governing Equations of Coupled Mode Theory

Coupled Mode Theory (CMT) starts with the description of how two interacting electromagnetic modes exchange energy in a photonic structure. Consider two optical modes propagating in adjacent

identical waveguides. The electric field in each waveguide can be represented by a slowly varying amplitude and a rapidly oscillating phase term:

$$E_1(z) = A_1(z)e^{i\beta_1 z}, \quad E_2(z) = A_2(z)e^{i\beta_2 z}$$

where A_1 and A_2 are the slowly varying amplitudes and β_1 and β_2 are the propagation constants of the modes in the two waveguides. In a simple idealized system (without asymmetries or loss), vc, these propagation constants are equal, $\beta_1 = \beta_2 = \beta$, meaning the modes are phase-matched and the energy transfer is highly efficient.

$$\beta = \frac{2\pi * n_{eff}}{\lambda_0}$$

The rate of energy exchange between the two waveguides is governed by the coupling coefficient κ, which depends on the overlap of the electromagnetic fields and the separation between the waveguides. The coupled mode equations for the slowly varying amplitudes are [26, 27]:

$$\frac{dA_1}{dz} = -i\kappa A_2 \tag{6.1}$$

$$\frac{dA_2}{dz} = -i\kappa A_1 \tag{6.2}$$

These equations describe the periodic exchange of energy between the two waveguides. In the ideal lossless case, the total power is conserved, and the power in each waveguide oscillates along the propagation direction. The coupling length, L_C, represents the distance over which the energy transfers completely from one waveguide to the other, and can be directly related to the coupling coefficient by [28]:

$$L_c = \frac{\pi}{2\kappa}$$

To demonstrate this phenomenon, a FDTD simulation was performed at $\lambda_0 = 1.55\ \mu m$, with two symmetric, 500 nm thick silicon nitride waveguides separated by a 1-micron gap, with vacuum permittivity as the background index. The results of the FDTD simulation were compared with the theoretical predictions from Coupled Mode Theory (CMT) by solving the coupled mode equations (6.1) and (6.2) numerically using a Python PDE solver. The coupling coefficient κ which governs the energy

exchange between the waveguides, was determined by fitting the numerical solution to the FDTD data. This was achieved by minimizing the residual between the FDTD power oscillation data and the numerical solution of the coupled PDEs.

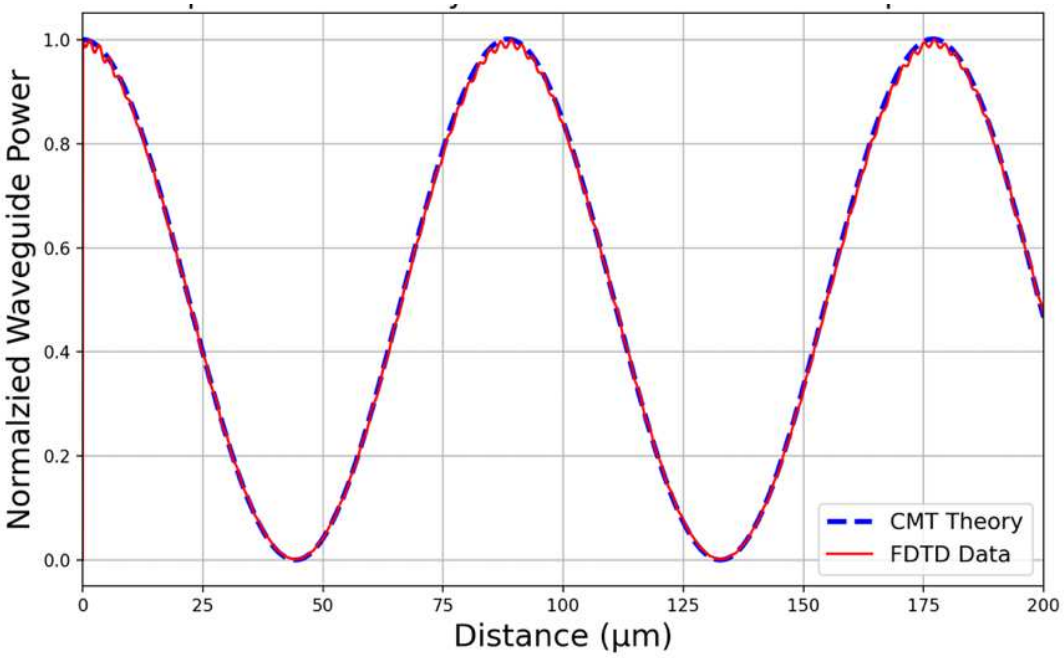

Figure 6.1: Comparison of theoretical predictions in one of two waveguides from Coupled Mode Theory (CMT) (blue dashed line) and results from a Finite-Difference Time-Domain (FDTD) simulation (red solid line). The two symmetric, 500 nm thick silicon nitride waveguides are separated by a 1 μm with a fitted coupling coefficient of $\kappa = 0.019\ \mu m^{-1}$

The coupling coefficient κ, which governs the frequency of power oscillations between the two waveguides, is directly proportional to the interaction strength between the waveguides. As the separation between the waveguides increases, κ decreases, resulting in a lower oscillation frequency. Conversely, reducing the separation strengthens the coupling and increases the oscillation frequency.

Although κ can be calculated from first principles using waveguide geometry and material properties, this method is computationally intensive. However, since the coupling length is clearly observable in Figure 6.1, the coupling parameters can be easily extracted from simulations by relating the coupling length to the coupling coefficient κ. This graphical approach provides an efficient alternative to direct computation, allowing the key parameters to be extracted from the simulation data without additional complexity.

6.2 Phase Mismatch and Resonant Coupling

In an ideal coupled mode system, two waveguides are phase-matched, meaning that their propagation constants β_1 and β_2 are identical. This condition leads to efficient energy transfer between the waveguides. However, in real-world systems, a phase mismatch often exists, where the propagation constants differ by

$$\Delta\beta = \beta_1 - \beta_2$$

Phase mismatch significantly impacts the energy transfer between waveguides. While a small phase mismatch allows for some energy exchange, the efficiency decreases as $\Delta\beta$ increases. In highly mismatched systems, the coupling becomes less effective, reducing the power transfer between the waveguides. The coupled mode equations, including phase mismatch, are given by [25, 26]:

$$\frac{dA_1}{dz} = -i\kappa e^{j\Delta\beta z} A_2 \tag{6.3}$$

$$\frac{dA_2}{dz} = -i\kappa e^{-j\Delta\beta z} A_1 \tag{6.4}$$

Here, A_1 and A_2 represent the modal amplitudes, κ is the coupling coefficient, and z is the propagation distance. The phase mismatch $\Delta\beta$ introduces an oscillatory phase shift between the modes, reducing the overall magnitude of the energy transfer. As a result, although the energy transfer remains oscillatory, the power exchanged is less, and not all the energy is fully transferred from one waveguide to the other. Importantly, the coupling length remains largely unchanged, but the amplitude of the power transfer decreases.

In this simulation, we introduce a phase mismatch by altering the dimensions of two silicon nitride (Si_3N_4) waveguides, both separated by 1 μm. Waveguide 1 has a width of 510 nm, while Waveguide 2 is 500 nm wide. The built-in mode solver reveals a small difference in effective indices:

$$n_{eff_1} = 1.507 \text{ and } n_{eff_2} = 1.5$$

This small difference in n_{eff} causes a phase mismatch between the modes, corresponding to $\Delta\beta \neq 0$. Figure 6.2 compares the results of the numerical solution of the coupled mode equations (solid red line) with

those from an FDTD simulation (dashed blue line). As seen in the figure, the coupling length is nearly identical to that of the phase-matched case (Figure 6.1); however, due to the phase mismatch, there is incomplete transmission of power between the waveguides. The FDTD simulation highlights the reduced coupling efficiency, confirming that as phase mismatch increases, a smaller fraction power is transferred between the two waveguides, even though the oscillatory behavior persists. The power initially launched into waveguide one and is normalized against the total power in both waveguides.

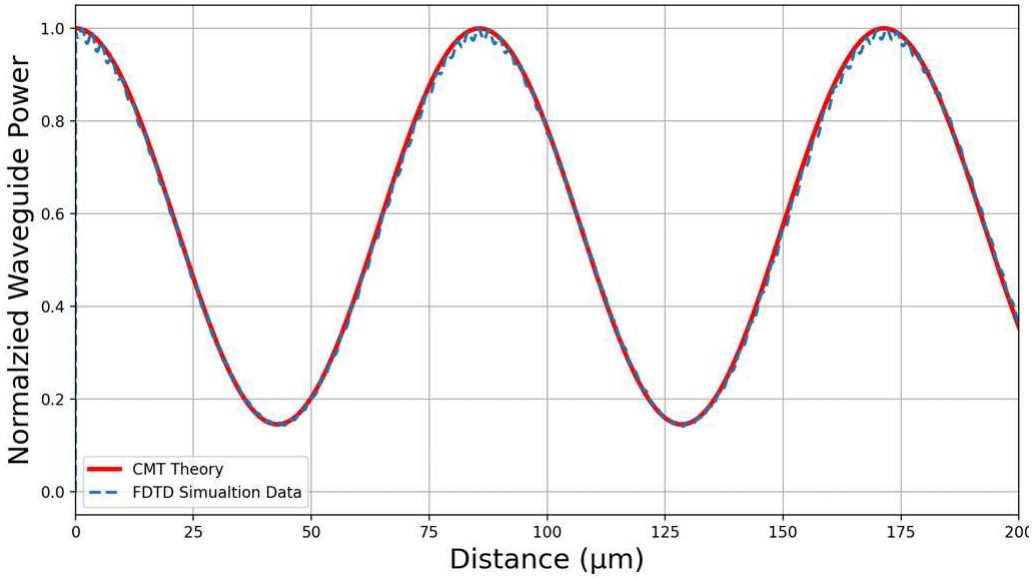

Figure 6.2: Comparison of theoretical predictions from Coupled Mode Theory (CMT) (solid red line) and results from a Finite-Difference Time-Domain (FDTD) simulation (dashed blue line) for two physically asymmetric Si_3N_4 waveguides. One 500 nm width and one 510 nm with a 1μm offset. The plot shows the power in the first waveguide. All power was initially launched into this waveguide, and the power is normalized to the total power in both waveguides.

6.3 Material Losses and Complex Coupling Coefficients

In practical waveguides, material losses due to absorption, scattering, or imperfections in fabrication are inevitable. These losses impact the energy transfer between waveguides and complicate the analysis of power distribution along the propagation path. To account for these effects, we introduce both a complex propagation constant and a complex coupling coefficient [26, 27]. In a lossless medium, the propagation constant β is real, indicating no attenuation. However, with material losses, β becomes complex:

$$\beta = \beta_r + i\alpha$$

where β_r is the real part of the propagation constant, and α is the imaginary part representing the attenuation coefficient. The power in the waveguide decays exponentially due to losses, and the electric field amplitude decreases as:

$$E(z) = E_0 e^{i\beta_r z} e^{-\alpha z}$$

Similarly, the coupling coefficient κ becomes complex when material losses are present. The complex coupling coefficient can be written as:

$$\kappa = \kappa_r + i\kappa_i$$

Here, κ_r is the real part of the coupling coefficient, responsible for the power exchange between the waveguides, and κ_i represents the imaginary part, which accounts for additional phase shifts and loss mechanisms introduced by the coupling process. In the presence of losses, the coupled mode remains the same only that the parameters can be complex [25, 26]:

$$\frac{dA_1}{dz} = -i\kappa e^{j\Delta\beta z} A_2$$

$$\frac{dA_2}{dz} = -i\kappa e^{-j\Delta\beta z} A_2$$

These equations describe the oscillatory transfer of energy between the waveguides, but now with attenuation due to the imaginary components of β and κ. As energy is transferred back and forth between the waveguides, the total power in the system gradually decreases due to material losses.

To validate this behavior, we performed an additional FDTD simulation using the same waveguide geometries described in Section 6.1: two silicon nitride waveguides, each 500 nm wide and separated by a 1 μm gap. A material loss was introduced into one waveguide by adding an imaginary component to its refractive index. To isolate the effects of material loss without introducing phase mismatch, we adjusted the real part of the refractive index to maintain the magnitude of the effective index values for both waveguides. This adjustment ensures that any phase shift caused by the loss is

compensated, allowing us to focus solely on energy attenuation. It was determined that under this geometry, the new effective indices were:

$$n_{eff_1} = 1.5 \text{ and } n_{eff_2} = 1.499 + 0.05i.$$

Figure 6.3 shows the comparison between the analytical solution of the coupled mode theory (CMT) and the FDTD simulation results. Both approaches reveal that the material loss, represented by the imaginary component of the refractive index, results in a reduction in the amplitude of the power oscillations between the waveguides. With each cycle of energy transfer, the total power in the system decreases, consistent with the exponential decay expected from the imaginary component of the refractive index. The power was launched into the lossless waveguide and the measured power is normalized against the total power in both waveguides.

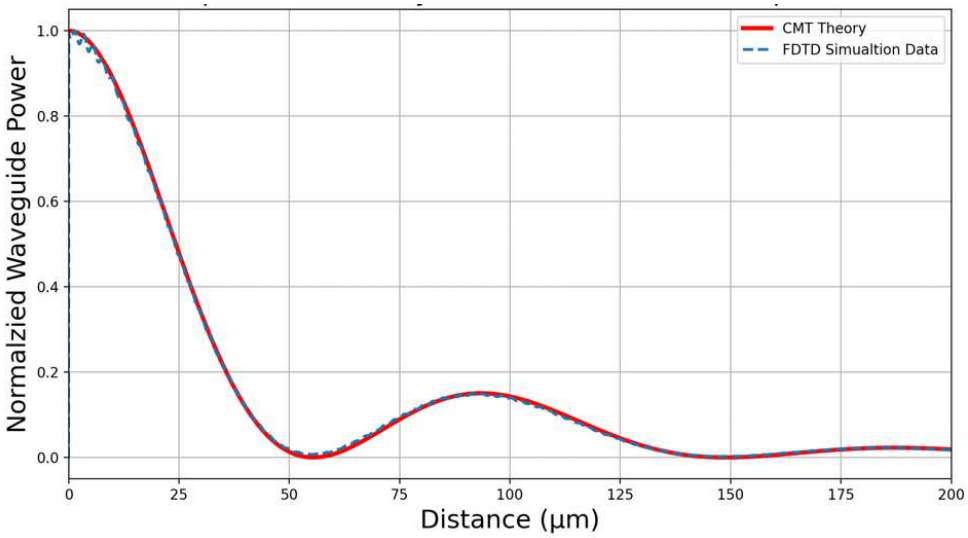

Figure 6.3: Comparison of Theoretical Predictions from Coupled Mode Theory and FDTD Simulations for Symmetric Waveguides with Slight Loss in One Waveguide. Power is launched and plotted against propagation distance for the lossless waveguide

To explore the effects of a larger refractive index mismatch, we performed a second simulation in which the effective index of the lossy waveguide was increased. In this case, the effective indices were:

$$n_{eff_1} = 1.5 \text{ and } n_{eff_2} = 4.0 + 0.05i.$$

Figure 6.4 compares the results from the coupled mode equations and the FDTD simulation for this scenario. Despite the presence of the same material loss, the large refractive index mismatch significantly limits the energy transfer between the waveguides. Consequently, very little power is lost to the lossy waveguide, as the strong phase shift due to the effective index difference prevents efficient coupling. This effect highlights the importance of phase matching for energy transfer in waveguide systems

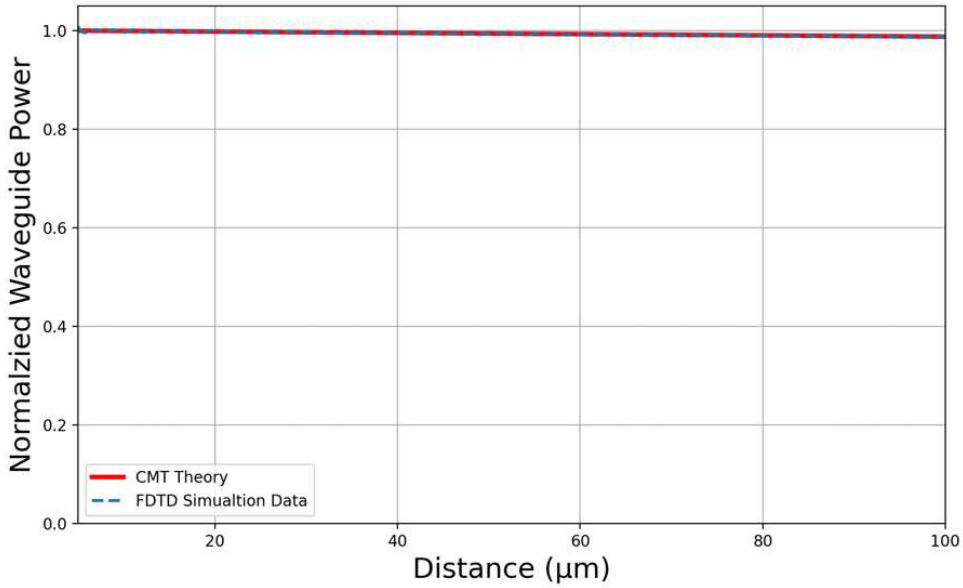

Figure 6.4: Comparison of CMT and FDTD Simulations for Symmetric Waveguides with Loss and a Large Effective Index Mismatch

6.4 Leaky Modes

Leaky modes occur when a portion of the guided wave in a waveguide escapes or "leaks" out of the waveguide core, typically due to weak confinement of the mode, the mode being unbound due to asymmetry of the cladding indices or being a higher order mode. These modes are characterized by a complex propagation constant, where the imaginary part represents the rate of attenuation as energy is lost from the waveguide. In contrast to bound modes, which are confined within the core and decay exponentially outside of it, leaky modes radiate energy into the surrounding cladding or substrate, leading to continuous energy loss along the propagation direction.

In the presence of leaky modes, the standard coupled mode equations must be adjusted to account for the independent loss experienced by each waveguide mode. While the coupling coefficient κ governs the energy exchange between the two waveguides, the loss associated with leaky modes is independent of this interaction and must be represented by an additional term [27]. The modified coupled mode equation becomes:

$$\frac{dA_1}{dz} = -i\kappa e^{j\Delta\beta z}A_2 - \gamma_1 A_1 \tag{6.5}$$

$$\frac{dA_2}{dz} = -i\kappa e^{-j\Delta\beta z}A_2 - \gamma_2 A_2 \tag{6.6}$$

Here, γ represents the decay constant associated with the leaky mode in each waveguide, independent of the coupling between the waveguides. This formulation ensures that the radiative loss is captured separately from the energy exchange between the waveguides, providing a more realistic description of how power decays in systems where leaky modes are present.

6.5 Extension to Complex Structures: LEAC Biosensor

While the previous sections have focused on relatively simple waveguide structures, more advanced photonic devices, such as the LEAC biosensor, introduce additional complexities that challenge the straightforward application of traditional Coupled Mode Theory (CMT). In the LEAC biosensor, energy transfer primarily occurs between the fundamental guided mode in the silicon nitride waveguide and various modes excited in the relatively thick germanium photodetector. Unlike the single-mode behavior of the waveguide, the photodetector can support a wide spectrum of higher-order modes, each with its own effective index and loss characteristics, complicating the overall energy transfer.

6.5.1: Effective Index of Higher Mode Orders

Using the Tidy3D mode solver, the first 100 TE modes supported by the nominal thickness of germanium photodetector were calculated. Figure 6.5 shows the effective magnitude of the real part of the effective index (n_{eff}) of each mode plotted against its mode index, along with the corresponding

magnitude of the imagine portion of the effective index (k_{eff}) which represents the attenuation of each mode due to loss.

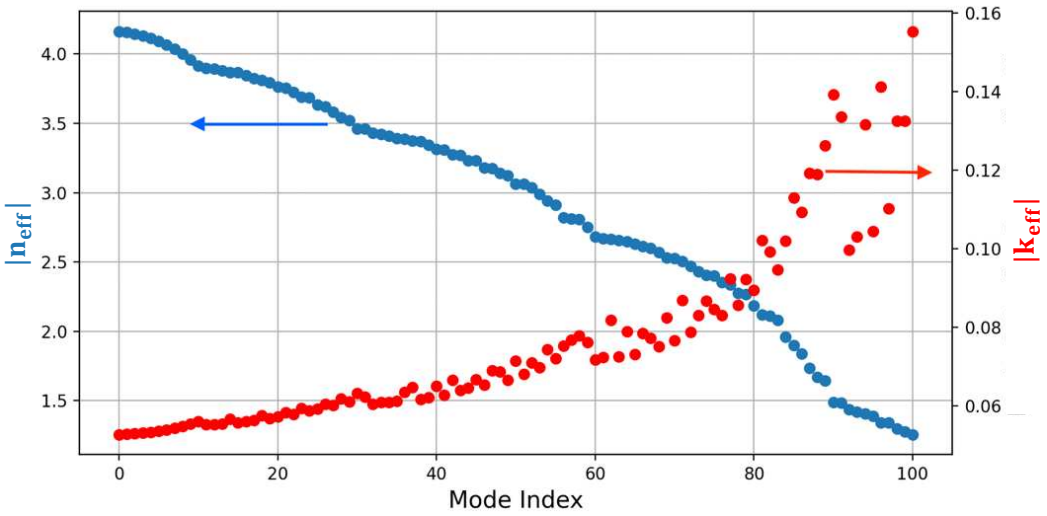

Figure 6.5: Mode magnitude of real and imaginary portion of the effective index vs. Mode Index for Higher-Order TE Modes in a nominally thick Germanium Photodetector

It is observed that the effective refractive index varies widely depending on the mode that is excited. This variation leads to a complex interplay of phase matching and coupling efficiency, as different modes can experience distinct coupling conditions. Some modes may phase match efficiently with the guided mode in the waveguide, while others may introduce significant phase mismatches, resulting in reduced energy transfer to the photodetector. In parallel, the effective extinction coefficient k_{eff} also shown in Figure 6.5, demonstrates how the effective detector absorption increases for higher-order modes. As the mode index increases, k_{eff} becomes larger, leading to more significant absorption losses for these higher-order modes. Interestingly, these modes also exhibit less phase mismatch, which can be interpreted as a form of resonance. While it might be tempting to explain this behavior in terms of mode confinement, higher-order modes are generally less confined. This reduced confinement occurs because higher-order modes have broader field distributions, extending further into the cladding or surrounding medium. As a result, they interact more with lossy regions outside the core, leading to

greater attenuation

6.5.2: Implication with LEAC Biosensor

The analysis of higher-order modes and their corresponding effective indices and extinction coefficients provides critical insights into the design and optimization of the LEAC biosensor. The interplay between phase matching and losses, as illustrated in Figure 6.5, presents a key challenge: the excitation of higher-order modes in the photodetector can lead to substantial absorption losses and mode beating. Section 4.4.3 highlights the dependence of detector sensitivity on photodetector thickness and presents results at resonant locations, where highly enhanced mode beating, and high absorption occur. Figure 4.6 shows the absorption as a function of PD thickness, overlaid with BPM simulations. The power versus propagation distance plots were taken for normalized detector thicknesses of 0.765 (on resonance) and 1 (off resonance).

First, considering the off-resonance case, it is evident that a higher-order mode is guided in the detector, as indicated by the multiple zero crossings, i.e. intensity nulls, along the y-axis. The lack of mode beating suggests a significant mismatch in the effective index between the SiN core mode and the PD mode. An effective index of 2.5 would result in sufficient phase mismatching to limit mode beating while still allowing for coupling to the PD and the loss of total mode power. In the resonant case there is still a higher order mode, and the effective index of the mode is much closer to the core effective index (1.5), as indicated by the oscillation of power along the propagation distance. The Mode solver simulation that was used to create data for Figure 6.5 was repeated for the mode with the smaller effective index. Based on the plot of mode effective index versus mode order, two modes were selected for further study: the 70^{th} mode with an effective index of 2.5 from Figure 6.5 and the 90^{th} mode with an index of 1.5 from data found for the thinner PD. Figure 6.6 shows the mode profiles for these two modes, with their effective index and effective extinction ratios plotted.

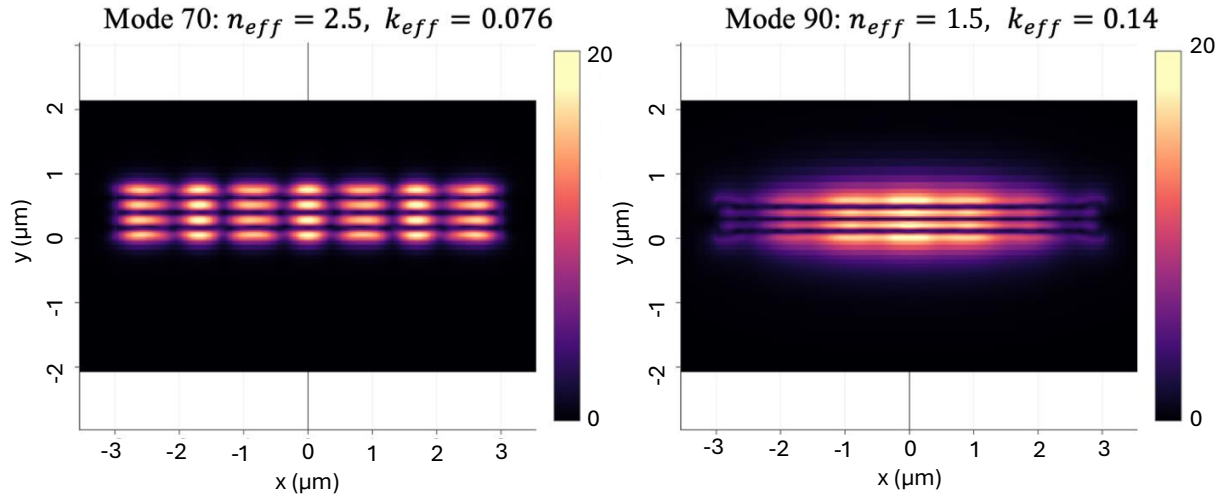

Figure 6.6: Mode Profiles for Higher- and Lower-Order Modes with Corresponding Effective Indices and Extinction Coefficients

The coupled mode equations were numerically solved using the same effective indices as the modes shown in Figure 6.6. The data from the BPM simulations, which show the core waveguide power versus propagation distance, were overlaid onto the CMT prediction. The CMT coupling coefficient was then fitted by minimizing the squared sum error between the BPM data and the analytical solution. The fitted coupling coefficients were found to be $0.021\ \mu m^{-1}$ for the resonant case and $0.071\ \mu m^{-1}$ for the off-resonant case.

Figure 6.6 shows there is substantial energy present in the off-resonant mode near the edge of the PD. The coupling coefficient depends on the overlap between the PD and core modes, and the difference between the two can be accounted for by this factor. Additionally, the BPM result for the "on resonance" PD in Figure 4.6 shows a coupling length of approximately 80 μm. The coupling coefficient for that coupling length is approximately $0.02\ \mu m^{-1}$. Figure 6.7 shows the comparison between the BPM simulation and the CMT analytical solution, illustrating the accuracy of the fit.

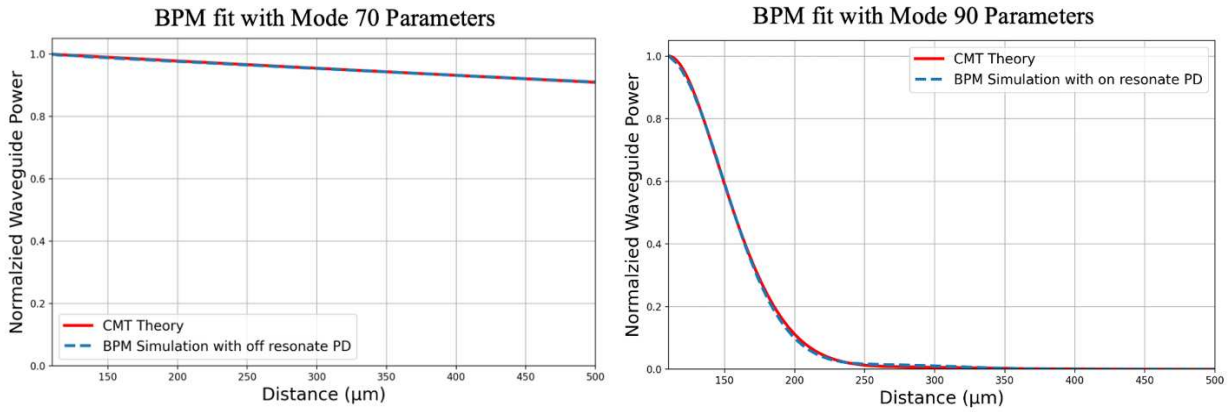

Figure 6.7: Comparison of BPM Simulations and CMT Predictions for Mode 70 (off-resonance) and Mode 90 (on-resonance) with PD starting at 100 μm

6.6 Conclusion

In this chapter, CMT is extended to address real-world complexities, including material losses, phase mismatch, and higher-order modes. By comparing CMT predictions with FDTD simulations, the model's ability to accurately capture power transfer dynamics in lossy environments is validated. The results show that small variations in effective index and material loss significantly affect coupling efficiency. Phase mismatches, caused by geometry or material differences, lead to reduced energy transfer and lower system efficiency.

The analysis of the LEAC biosensor highlights the practical impact of these findings. Higher-order modes in the germanium photodetector, influenced by effective index and extinction coefficient variations, directly affect sensor performance. Resonant conditions at certain thicknesses enhance absorption, while phase mismatches reduce energy transfer. This work provides critical insights for optimizing photonic devices, offering a path to improved performance and reduced losses, applicable to both simple waveguide systems and more complex structures like the LEAC biosensor.

CHAPTER 7 - CONCLUSION

This thesis presented an in-depth investigation into the performance and manufacturability of Local Evanescent Array Coupled (LEAC) biosensors using a combination of Beam Propagation Method (BPM) and Finite-Difference Time-Domain (FDTD) simulations. The primary goal was to explore how variations in key design parameters, such as waveguide core thickness, cladding layers, and photodetector placement, affect sensor sensitivity and crosstalk in multi-region sensors.

7.1 Key Findings

LEAC biosensor sensitivity is primarily dictated by the waveguide core thickness. Thinner cores increase sensitivity by extending the evanescent field further into the sensing region. However, thin cores also pose fabrication challenges and reduce repeatability. However, a 25 nm error in core thickness caused less than a 10% shift in sensitivity, demonstrating the design's tolerance to manufacturing variations.

Cladding thickness also impacts sensitivity. Contrary to expectations, thicker cladding increases sensitivity due to the interaction between the photodetector and the extended evanescent field. A 300 nm error in the lower cladding resulted in less than a 10% change in sensitivity. However, tighter tolerances are needed for the photodetector to avoid performance degradation. Resonant absorption between the core and the photodetector can enhance sensitivity, but a 10% error in photodetector thickness at resonance can cause a 600% change in sensitivity. Off-resonance, the same error in photodetector thickness has minimal impact.

Crosstalk was quantified using FDTD simulations and photocurrent ratios to assess both forward and reverse crosstalk by comparing local region dependencies with upstream or downstream sensing regions. Photocurrent ratios effectively eliminated forward crosstalk, particularly in bulk samples, where power dissipation and flux modulation were significant. However, this approach introduced a dependence

on downstream samples, leading to reverse crosstalk. In contrast, using absolute photocurrents in the crosstalk ratios mitigated reverse crosstalk, minimizing its impact. Monolayer samples exhibited negligible forward crosstalk, and reverse crosstalk, caused by reflections at dielectric boundaries, remained low in both bulk and monolayer samples when absolute current values were used.

7.2 Practical Implications for Manufacturing

This study has significant implications for the large-scale fabrication of LEAC biosensors. One of the core challenges in transitioning from research to mass production is the ability to maintain tight tolerances in waveguide and photodetector dimensions. Our tolerance analysis revealed that even small deviations in these parameters can have a substantial impact on sensor performance, particularly with respect to resonant phenomena. To address this, we proposed a modified structure that flattens the sensitivity curve across a broader range of photodetector thicknesses, making the device more resilient to manufacturing imperfections. This adjustment is critical for ensuring consistent performance across large production batches, especially in applications such as point-of-care diagnostics and environmental monitoring where high throughput is essential.

7.3 Limitations and Future Work

While this study provides a detailed analysis of LEAC biosensor performance, several limitations should be noted. The reliance on simulation methods such as BPM and FDTD introduces assumptions about device structure and operational conditions that may not fully reflect real-world variability, such as environmental factors like temperature, humidity, and mechanical stress. Future work should prioritize experimental validation of these findings by testing biosensors in varied environmental conditions to assess real-world robustness and performance. It is important to conduct experiments that measure the sensor’s sensitivity to coupling loss, surface roughness, and waveguide imperfections, as these factors were not extensively covered in the simulations. Controlled experiments in environments with fluctuating temperatures and mechanical vibrations will provide deeper insights into the sensor’s durability and stability. Furthermore, evaluating the biosensor's performance over extended periods in biological media will be crucial to understanding long-term reliability for practical applications.

Another critical area for future investigation is the role of electrical noise. Experiments should determine whether the LEAC biosensor is primarily limited by shot noise or if other noise sources, such as thermal or environmental noise, are more dominant. Measuring the photocurrent generated under different operational conditions will help determine the sensitivity threshold of the device. This, in turn, will guide the optimization of the sensor for specific diagnostic applications where noise control is critical. To fully understand the tolerance of the biosensor design, the next step will be to manufacture and characterize a batch of sensors. These tests should evaluate performance against the specified tolerances to validate the design parameters and ensure consistency across multiple sensors. Insights from this experimental round will be key to refining the design for commercial-scale manufacturing.

In conclusion, this thesis has provided valuable insights into the design and optimization of LEAC biosensors, paving the way for scalable manufacturing. By examining the relationships between waveguide dimensions, photodetector properties, and sensor performance, we have outlined a clear path for future advancements. As biosensing technologies evolve, the LEAC biosensor holds great promise for high-sensitivity, low-cost diagnostics across a range of applications.

.

REFERENCES

[1] Carrell C, Link J, Jang I, Terry J, Scherman M, Call Z, et al. Point-of-Need Disposable ELISA System for COVID-19 Serology Testing. ChemRxiv. 2021; doi:10.26434/chemrxiv-2021-c4bmd-v3 This content is a preprint and has not been peer-reviewed.

[2] Yan, R., Mestas, S. P., Yuan, G., Safaisini, R., Dandy, D. S., & Lear, K. L. (2009). Label-free silicon photonic biosensor system with integrated detector array. Lab on a Chip, 9(15), 2163. https://doi.org/10.1039/b902111f

[3] T. A. Erickson and K. L. Lear, "Optimization of the Local Evanescent Array-Coupled Optoelectronic Sensing Chip for Enhanced, Portable, Real-Time Sensing," in IEEE Sensors Journal, vol. 13, no. 5, pp. 1905-1913, May 2013, doi: 10.1109/JSEN.2013.2242058.

[4] Khan AR, Hussain WL, Shum HC and Hassan SU (2024), Point-of-care testing: a critical analysis of the market and future trends. Front. Lab. Chip. Technol. 3:1394752. doi: 10.3389/frlct.2024.1394752

[5] Chen, C., & Wang, J. (2020). Optical biosensors: An exhaustive and Comprehensive Review. The Analyst, 145(5), 1605–1628. https://doi.org/10.1039/c9an01998g

[6] Prabowo BA, Purwidyantri A, Liu K-C. Surface Plasmon Resonance Optical Sensor: A Review on Light Source Technology. Biosensors. 2018; 8(3):80. https://doi.org/10.3390/bios8030080

[7] Chen, Y., Ming, H. Review of surface plasmon resonance and localized surface plasmon resonance sensor. Photonic Sens 2, 37–49 (2012). https://doi.org/10.1007/s13320-011-0051-2

[8] Prieto, F., Sep lveda, B., Calle, A., Llobera, A., Dom nguez, C., Abad, A., Montoya, A., & Lechuga, L. M. (2003). An integrated optical interferometric nanodevice based on silicon technology for Biosensor Applications. Nanotechnology, 14(8), 907–912. https://doi.org/10.1088/0957-4484/14/8/312

[9] Schmitt, K., Schirmer, B., Hoffmann, C., Brandenburg, A., & Meyrueis, P. (2007). Interferometric biosensor based on planar optical waveguide sensor chips for label-free detection of Surface Bound Bioreactions. Biosensors and Bioelectronics, 22(11), 2591–2597. https://doi.org/10.1016/j.bios.2006.10.016

[10] Nordin A. Optical-resonator-based biosensing systems: status and future prospects. Nanobiosensors in Disease Diagnosis. 2016;5:41-50 https://doi.org/10.2147/NDD.S70385

[11] Guider, R., Gandolfi, D., Chalyan, T., Pasquardini, L., Samusenko, A., Pederzolli, C., Pucker, G., & Pavesi, L. (2015). Sensitivity and limit of detection of biosensors based on ring resonators. Sensing and Bio-Sensing Research, 6, 99–102. https://doi.org/10.1016/j.sbsr.2015.08.002

[12] Verma, Y. K., Kumari, S., Bawa, G., & Tripathi, S. M. (2022). Temperature insensitive large free spectral range micro-ring resonator. Optical and Quantum Electronics, 54(12). https://doi.org/10.1007/s11082-022-04266-7

[13] Guangwei Yuan, K. L. Lear, M. D. Stephens and D. S. Dandy, "Initial demonstration of a local, evanescent, array coupled biosensor concept," SENSORS, 2005 IEEE, Irvine, CA, USA, 2005, pp. 4 pp.-, doi: 10.1109/ICSENS.2005.1597847.

[14] Ardoino N, Lunelli L, Pucker G, Vanzetti L, Favaretto R, Pasquardini L, Pederzolli C, Guardiani C, Potrich C. Optimization of Surface Functionalizations for Ring Resonator-Based Biosensors. Sensors. 2024; 24(10):3107. https://doi.org/10.3390/s24103107

[15] Huraiya, M. A., Razzak, S. M., Tabata, H., & Ramaraj, S. G. (2024). New approach for a highly sensitive V-shaped SPR biosensor for a wide range of analyte ri detection. The Journal of Physical Chemistry C. https://doi.org/10.1021/acs.jpcc.4c04425

[16] Synopsis. (2023). 2: Background . In Photonic Solutions BeamPROP PBM (V2023.03, pp. 14–25). essay, Synopsis Inc. .

[17] Huang, W. P., & Xu, C. L. (1993). Simulation of three-dimensional optical waveguides by a full-vector beam propagation method. IEEE Journal of Quantum Electronics, 29(10), 2639–2649. https://doi.org/10.1109/3.250386

[18] Hongling Rao, Scarmozzino, R., & Osgood, R. M. (1999). A bidirectional beam propagation method for multiple dielectric interfaces. IEEE Photonics Technology Letters, 11(7), 830–832. https://doi.org/10.1109/68.769722

[19] Peatross, J., & Ware, M. (2023). Physics of light and Optics. Brigham Young University, Department of Physics.

[20] Chen, C.-L. (2007). BRIEF REVIEW OF ELECTROMAGNETICS AND GUIDED WAVES. In FOUNDATIONS FOR GUIDED-WAVE OPTICS (pp. 1–25). essay, John Wiley & Sons.

[21] Fan, S., Hughes, T., & Yu, Z. (2022, April 15). FDTD method introduction: Lecture 1 flexcompute. Flexcompute. https://www.flexcompute.com/fdtd101/Lecture-1-Introduction-to-FDTD-Simulation/

[22] Gedney, S. D., & Balanis, C. A. (2011). Introduction to the finite-difference time-domain (FDTD) method for electromagnetics (1st ed., Vol. 27). In Yee Algorithm for Maxwell's Equations (pp. 39-52). Morgan & Claypool Publishers.

[23] Holmes, C. D., & Lear, K. L. (2024). Tolerance analysis of local evanescent array coupled (LEAC) sensors fabricated in Silicon Photonics Foundries. Physics and Simulation of Optoelectronic Devices XXXII, 17. https://doi.org/10.1117/12.3009540

[24] Erickson TA, Nijjar R, Kipper MJ, Lear KL. Characterization of plasma-enhanced teflon AF for sensing benzene, toluene, and xylenes in water with near-IR surface plasmon resonance. Talanta. 2014 Feb;119:151-5. doi: 10.1016/j.talanta.2013.10.038. Epub 2013 Oct 24. PMID: 24401397.

[25] Haus, H., Huang, W., Kawakami, S., & Whitaker, N. (1987). Coupled-mode theory of optical waveguides. Journal of Lightwave Technology, 5(1), 16–23. https://doi.org/10.1109/jlt.1987.1075416

[26] Teich, M. C., & Saleh, B. E. A. (1991a). B. Coupling Between Waveguides. In Fundamentals of Photonics (pp. 264–270). essay, Wiley.

[27] Christopoulos, T., Tsilipakos, O., & Kriezis, E. E. (2024). Temporal coupled-mode theory in nonlinear resonant photonics: From basic principles to contemporary systems with 2D materials, dispersion, loss, and gain. Journal of Applied Physics, 136(1). https://doi.org/10.1063/5.0190631

APPENDIX A – DERIVATION OF WAVE EQUATION

To fully grasp the operational principles of a Local Evanescent Array Coupled (LEAC) biosensor, it is essential to start with the fundamentals of light propagation within a slab waveguide. A typical slab waveguide consists of a high refractive index core surrounded by lower refractive index cladding layers ($n_1 > n_2 \geq n_3$), facilitating the confinement and guidance of light through total internal reflection at the core-cladding interfaces. Coordinate conventions for defining waveguide geometry vary widely from source to source. Figure 1.1 will illustrate a cross-section of this slab waveguide, showing the core and cladding layers with dimensions oriented along the z-axis (propagation direction), x-axis (transverse direction), and y-axis (normal to the wafer). Figure 1.2 will further detail the boundaries where the evanescent field forms, highlighting the transition of the refractive index from the core to the cladding. These figures are integral in visualizing the physical geometry and refractive index profiles essential for understanding how bound modes are formed and maintained within the waveguide. The modes in which light propagates within the waveguide can be described as a combination of propagating waves along the z-direction, which is the direction of waveguide length, and standing waves that exhibit oscillatory behavior in the core and decay exponentially in the cladding, manifesting as evanescent tails.

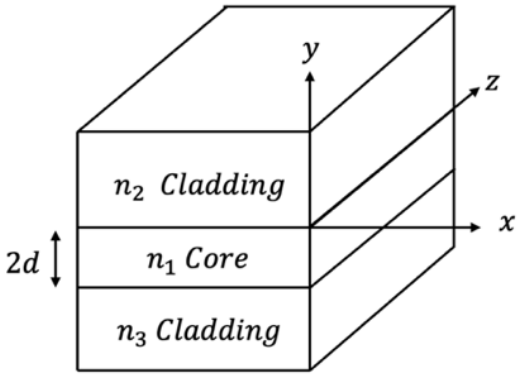

Figure A1: Refractive index profile for three-dimensional slab waveguide with the z-axis as the propagation direction, x-axis as the transverse direction, and y-axis as the axis normal to the wafer surface.

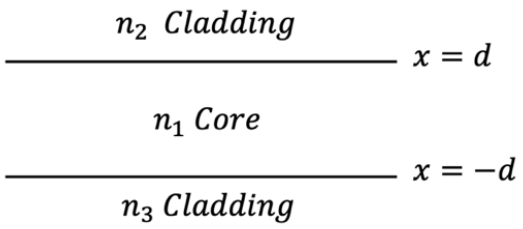

Figure A2: Dimensions of a three-dimensional slab waveguide

Referring to the waveguide configurations outlined in figure 1.1, Maxwell's equations can be invoked to solve for transverse electric field profile of the waveguide. For TE modes, only the E_z component of the electric field is non-zero. Maxwell's equations in the absence of free charges and currents simplify to:

$$\vec{\nabla} \times \vec{E} = i\omega\mu H \tag{1.5}$$

$$\vec{\nabla} \times \vec{H} = -i\omega\epsilon E \tag{1.6}$$

By taking the curl of equation 1.5 and substituting from equation 1.6, we obtain the wave equation for the electric field by employing the curl-on-curl vector identity:

$$\nabla \times (\nabla \times E) = \nabla(\nabla \cdot E) - \nabla^2 E$$

Since $\nabla \cdot E = 0$ in an isotropic medium, we can simplify to:

$$\nabla \times (\nabla \times E) = -\nabla^2 E$$

Substituting from equation 1.6:

$$\nabla \times (i\omega\mu H) = -\nabla^2 E$$

$$i\omega\mu(-i\omega\epsilon E) = -\nabla^2 E$$

$$\nabla^2 E - \omega^2 \mu\epsilon E = 0$$

If $\epsilon = \epsilon_0 n^2$, we get the final equation:

$$\nabla^2 E + k_0^2 n^2 E = 0 \tag{1.7}$$

Where $k_0 = \frac{\omega}{c}$ is the wave number in free space. For the TE mode in a slab waveguide, we assume the electric field has only a z-component. The wave equation (2.7) for E_z becomes:

$$\frac{\partial^2 E_z}{\partial x^2} + \frac{\partial^2 E_z}{\partial y^2} + k_0^2 n^2 E_z = 0 \tag{1.8}$$

We assume the field varies infinitely in the x-direction, meaning that we can write the solution to the equation of the form $E_z(y,z) = E_y(y)e^{i\beta z}$. The propagation constant β is a critical parameter in waveguide theory, determining the confinement and propagation characteristics of the guided mode. It dictates the rate at which the phase of the wave changes along the propagation direction z, with the term $e^{i\beta z}$. indicating a linear phase change proportional to β. In free space, the wavenumber k_0 is defined as $k_0 = \frac{\omega}{c}$, while in a waveguide, β is related to the effective refractive index n_{eff} by $\beta = k_0 n_{eff}$, where n_{eff} is the effective refractive index experienced by the mode [4]. For a mode to be guided, β must lie between the wavenumbers of the core and cladding materials, $k_0 n_2 < \beta < k_0 n_1$, ensuring that the wave is confined to the core and decays exponentially in the cladding regions. In the cladding β becomes complex due to the lower refractive index n_2 and its imaginary part leads to an exponential decay of the field, forming evanescent tails. This indicates that the wave does not propagate in the cladding but rather forms a standing wave that attenuates as it moves away from the core-cladding interface. We obtain the ordinary differential equation 1.8. We can now split the solution to the ODE between the core and cladding region.

Core Region ($0 < y < d$):

$$\frac{\partial^2 E_z}{\partial y^2} + (k_0^2 n^2 - \beta^2) E_y = 0 \tag{1.9}$$

Let $k_1^2 = k_0^2 n_{core}^2 - \beta^2$, we then have the solution:

$$E_y(y) = A\cos(k_1 y) + B\sin(k_1 y)$$

Cladding Regions ($y < 0$ & $y > d$):

$$\frac{\partial^2 E_z}{\partial y^2} + (k_0^2 n^2 - \beta^2) E_y = 0 \tag{1.10}$$

Let $\alpha^2 = \beta^2 - k_0^2 n_{clad}^2$, we then have the solution:

$$E_y(y) = Ce^{\alpha y} \text{ for } y > 0 \tag{1.11}$$

$$E_y(y) = De^{-\alpha(y-d)} \text{ for } y < 0 \tag{1.12}$$

Boundary conditions can then be applied at $y = d$ & $y = 0$ to ensure that the field is continuous over the dielectric boundary. This configuration supports the confinement and guidance of light along the waveguide due to total internal reflection (TIR) at the core-cladding interface. The behavior of light in waveguides can be described by the wave equation. For a guided mode, the solution to this equation in the core is typically oscillatory, indicating propagating waves. In the cladding, the propagation constant β (a component of the wave vector along the direction of propagation) becomes complex due to the lower refractive index. The imaginary part of β leads to an exponential decay of the wave's amplitude in the cladding. The presence of this imaginary component indicates that the wave does not propagate in the cladding but rather forms a standing wave that attenuates as it travels away from the core-cladding interface.

The evanescent field, which extends from the core into the cladding of the device, is crucial for the operation of LEAC biosensors. This field decays exponentially and its penetration depth d_p is influenced by the refractive index contrast between the core and cladding materials. The wave equation in the cladding is given by equation 1.8. For an exponentially decaying field in the cladding, the solution is:

$$E_y(y) = E_0 e^{-\alpha y} \tag{1.13}$$

Where α is the decay constant. Substituting into the wave equation gives:

$$\alpha^2 E_0 e^{-\alpha y} + (k_0^2 n^2 - \beta^2) E_0 e^{-\alpha y} = 0$$

Simplifying:

$$\alpha^2 + k_0^2 n^2 - \beta^2 = 0$$

Thus,

$$\alpha^2 = \beta^2 - k_0^2 n_{clad}^2$$

The penetration depth is the reciprocal of α

$$d_p = \frac{1}{\alpha} = \frac{1}{\sqrt{\beta^2 - k_0^2 n_{clad}^2}}$$

Using $\beta = k_0 n_{eff}$:

$$d_p = \frac{1}{\sqrt{(k_0 n_{eff})^2 - k_0^2 n_{clad}^2}} = \frac{\lambda_0}{2\pi} \frac{1}{\sqrt{n_{eff}^2 - n_{clad}^2}} \tag{1.14}$$

The evanescent field's penetration depth determines how effectively it interacts with the photodetector located beneath the waveguide, which is crucial for the sensor's performance. The penetration depth d_p affects how far the evanescent field extends into the lower cladding and how much of it reaches the photodetector; a deeper penetration increases the interaction with the photodetector. In LEAC biosensors, the refractive index of the upper cladding changes due to the sample. This change modulates the evanescent tail in the lower cladding. When the upper cladding's refractive index $n_{2,upper}$ increases, the effective index n_{eff} shifts, altering the penetration depth into the lower cladding. This modulation affects the intensity of the evanescent field at the photodetector, enabling the detection of small changes in the sample's refractive index.

APPENDIX B – USING TIDY3D

This appendix serves as a detailed manual for setting up and running optical simulations using Tidy3D. It is designed to provide future students with in-depth knowledge of the components used in Tidy3D simulations, their applications, and additional functionalities that can be explored in more complex scenarios

B.1 Introduction to Tidy3D

Tidy3D is a flexible and powerful electromagnetic simulation tool that uses the Finite-Difference Time-Domain (FDTD) method to solve Maxwell's equations. It is highly suitable for photonic simulations involving waveguides, resonators, and biosensors. The tool allows for defining custom materials, creating complex geometries, and studying how light interacts with different structures. This guide will focus on how to use Tidy3D for optical simulations, though the techniques and components discussed are applicable to a wide range of electromagnetic simulations.

B.2 Initialization and Simulation Environment

Before any simulation is run, the user needs to initialize the simulation environment. This involves setting the fundamental parameters, including the operating wavelength, simulation time, and device dimensions. In Tidy3D, initialization typically begins with defining these variables.

```
import tidy3d as td
from tidy3d import web
import matplotlib.pyplot as plt

# Set free-space wavelength (in micrometers) and corresponding frequency (in Hz)
lambda0 = 1.55  # Free-space wavelength in micrometers
freq0 = td.C_0 / lambda0  # Frequency derived from wavelength using speed of light
fwidth = freq0 / 10  # Frequency width for source

# Define device dimensions
wg_width = 7.0  # Waveguide width in micrometers
wg_thickness = 0.125  # Waveguide thickness in micrometers
pd_thickness = 0.7825  # Photodetector thickness in micrometers
domain_length = 450  # Total length of the simulation domain
```

Key Parameters:

- Wavelength (λ_0)Defines the operating wavelength of the light in the simulation. This must be consistent with the intended operating conditions of the optical device.
- Frequency (f_0): Calculated from the wavelength using $f_0 = \frac{c}{\lambda_0}$, where c is the speed of light.
- Domain Dimensions: Refers to the size of the simulation region, which must encapsulate the entire device and the surrounding space.

What else can be done?

- Custom Frequency Sweeps: Users can simulate multiple frequencies to study the device's behavior across a wide range of wavelengths, which is useful for resonators or broadband applications.
- Polarization Control: The simulation can be configured to study TE, TM, or mixed polarizations, providing flexibility in the types of modes launched into the waveguide.

B.3 Defining Materials

Tidy3D allows for the precise definition of materials, which is critical for capturing the optical properties of the device under test. Materials can be dispersive (frequency-dependent), anisotropic, or lossless.

Example Material Definitions:

```
# Silicon Nitride (Si3N4) for waveguide core
medium_SiN = td.PoleResidue(
    name='Silicon Nitride',
    frequency_range=[1e14, 7e14],  # Frequency range for which this material is valid
    eps_inf=3.031,  # Infinite frequency permittivity
    poles=[[(0-7.5e13j), (0+3.5e13j)]]  # Defines dispersion using pole-residue model
)
# Germanium (Ge) for photodetector
medium_Ge = td.Medium(name='Germanium', permittivity=18.3)
# Water as surrounding medium
medium_Water = td.Medium(name='Water', permittivity=1.77)
```

Material Properties:

- Permittivity (ε): This defines how light propagates through the material. For dispersive materials, a frequency-dependent model such as the Pole-Residue method is used to account for variations in permittivity across frequencies.
- Poles and Residues: These parameters model material dispersion, especially for materials like silicon or germanium, where refractive index varies with frequency.
- Lossy Materials: Materials such as metals or doped semiconductors can have both permittivity and conductivity defined, capturing their absorptive properties.

What else can be done?

- Anisotropic Materials: Users can define anisotropic materials (e.g., birefringent materials) where the refractive index varies with direction. This is useful for materials like liquid crystals or certain crystals used in nonlinear optics.
- Custom Models: Tidy3D supports custom dispersive models for materials not already included in its database, which is useful for specialized applications.

B.4 Defining Structures

The td.Structure class is used to create the geometric representation of devices such as waveguides, photodetectors, and cladding layers.

Example Structure Definitions:

```
# Define the waveguide as a rectangular box
Waveguide = td.Structure(
    geometry=td.Box(center=[0, 0, 0], size=[500, wg_width, wg_thickness]),
    medium=medium_SiN  # Silicon Nitride material
)
# Define the photodetector as a rectangular box below the waveguide
Ge_Detector = td.Structure(
    geometry=td.Box(center=[50, 0, -1.85], size=[150, 7.5, pd_thickness]),
    medium=medium_Ge  # Germanium material
)
```

Geometric Definitions:

- Box: The simplest geometry used to define rectangular structures, such as waveguides or cladding layers.
- Center and Size: Specify the center coordinates and the size in xxx, yyy, and zzz directions.

What else can be done?

- Complex Geometries: Tidy3D allows for more complex shapes like cylinders, spheres, and custom geometries using Boolean operations. This is useful for designing microstructures such as gratings or photonic crystals.
- Parametric Sweeps: Users can perform parametric sweeps, adjusting the size or position of structures to study design sensitivities or optimize device performance.

B.5 Creating Sources and Monitors

In Tidy3D, sources are used to inject electromagnetic waves into the simulation, while monitors capture field distributions, power flux, and other parameters for analysis. A field monitor is particularly useful for capturing detailed spatial distributions of electric or magnetic fields, which can help visualize mode profiles, resonances, and the evolution of fields throughout the simulation.

```
# Define a mode source injecting light into the waveguide
source = td.ModeSource(
    name='Input Source',
    center=[-50, 0, 0],
    size=[0, 8, 5],
    source_time=td.GaussianPulse(freq0=freq0, fwidth=fwidth),  # Gaussian pulse centered at freq0
    direction='+',  # Forward direction
    mode_spec=td.ModeSpec(filter_pol='te')  # TE-polarized mode
)
# Define a field monitor to capture the electric field distribution
field_monitor = td.FieldMonitor(
    name='Electric Field Monitor',
    center=[50, 0, 0],  # Monitor positioned at 50 um along the waveguide
    size=[100, 7, 5],  # Monitor region size to capture the field over a cross-section
    freqs=[freq0],  # Frequency of the field to monitor
    fields=['E'],  # Monitor the electric field
    output='abs'  # Absolute value of the electric field
)
```

Source Types:

- Mode Sources: Inject specific modes (TE, TM, or hybrid) into waveguides. Users can define the polarization (TE or TM) and the mode profile (fundamental, higher order).
- Point and Plane Sources: Useful for injecting light over a point or plane, allowing for broader excitation of the simulation space.

Monitor Types:

- Field Monitors: Capture the spatial distribution of electric or magnetic fields at defined regions. These are useful for visualizing how the field propagates through waveguides or how it interacts with different device components. The field monitor can output components such as E_x, E_y, E_z or the absolute values (e.g., |E||) of the electric field.

What else can be done with Field Monitors?

- Time-Domain Tracking: Field monitors can capture the time-domain evolution of the fields, allowing for the study of transient effects in pulsed systems or switching devices.
- Magnetic Field Monitoring: Field monitors can also be configured to capture the magnetic field components, providing a complete picture of the electromagnetic field dynamics.
- Field Slices and Volumes: Field monitors can be set to capture slices or volumes of the simulation space, offering flexibility in studying fields at specific cross-sections or over extended regions.

Visualization of Field Results:

```
# Retrieve the simulation data
sim_data = td.SimulationData.from_file('path_to_simulation_data.hdf5')
# Plot the electric field from the field monitor
fig, ax = plt.subplots(figsize=(10, 6))
sim_data.plot_field('Electric Field Monitor', 'E', 'abs', ax=ax)
ax.set_title('Electric Field Distribution Along Waveguide')
plt.show()
```

Once the simulation is complete, field data can be visualized to examine the distribution of the electric or magnetic fields in the simulation domain. Here's an example of how to visualize the electric field captured by the field monitor:

B.6 Running and Managing Simulations

Once the sources, monitors, and structures are defined, the next step is to configure and run the simulation. Tidy3D allows users to either run the simulation locally or upload it to Tidy3D's cloud platform for processing.

```
# Set up the simulation
sim = td.Simulation(
    center=[0, 0, 0],  # Center of the simulation domain
    size=[200, 10, 5],  # Size of the simulation domain (x, y, z)
    grid_spec=td.GridSpec(
        grid_x=td.AutoGrid(min_steps_per_wvl=6),  # Grid resolution in x-axis
        grid_y=td.AutoGrid(min_steps_per_wvl=6),  # Grid resolution in y-axis
        grid_z=td.AutoGrid(min_steps_per_wvl=14),  # Higher resolution in z-axis
    ),
    run_time=3.5e-12,  # Simulation runtime in seconds (based on the pulse width and waveguide
length)
    medium=td.Medium(name='Background', permittivity=1.0),  # Background medium (air or
vacuum)
    sources=[source],  # Defined sources
    monitors=[field_monitor],  # Field monitor to capture results
    structures=[Waveguide, Ge_Detector, Water_Cladding]  # Structures defined earlier
)
# Upload and run the simulation on Tidy3D's cloud platform
sim_data = web.run(sim, task_name='LEAC Biosensor Simulation')
```

Key Simulation Components:

- Simulation Domain: Defines the size and center of the region in which the simulation takes place. It must be large enough to contain all structures and allow the fields to propagate without interacting with the boundaries.
- Grid Specification: Defines the resolution of the simulation grid. A higher number of grid points per wavelength ensures more accurate results but requires more computational resources.
- Run Time: The time for which the simulation runs. This depends on the pulse width, device length, and how long the fields need to propagate within the structure.

What else can be done?

- Custom Grid Spacing: For more complex simulations or structures with fine details, users can manually specify grid spacing using ManualGrid instead of AutoGrid, giving finer control over grid resolution in specific regions.
- Boundary Conditions: Tidy3D automatically applies perfectly matched layers (PMLs) to the boundaries, ensuring that fields leaving the simulation domain do not reflect back. Users can customize boundary conditions for special cases like periodic or symmetric structures.
- Batch Simulations: Multiple simulations with varying parameters (e.g., material properties, structure dimensions) can be run in batch mode, allowing for parametric sweeps or optimizations across different configurations.

B.7 Retrieving and Analyzing Simulation Results

After the simulation completes, the data can be retrieved and analyzed using Tidy3D's API. Results typically include the field distributions, flux measurements, or other quantities captured by the monitors.

Example of Retrieving Results:

```
# Load simulation data from the saved file
sim_data = td.SimulationData.from_file('path_to_simulation_data.hdf5')
# Retrieve the electric field data from the field monitor
field_values = sim_data['Electric Field Monitor'].fields['E']
# Plot the electric field magnitude
fig, ax = plt.subplots(figsize=(10, 6))
sim_data.plot_field('Electric Field Monitor', 'E', 'abs', ax=ax)
ax.set_title('Electric Field Distribution')
plt.show()
```

Analyzing Field Data:

- Electric Field Distributions: The field monitor captures the electric field at specific points in the simulation domain. These can be visualized to examine how the light propagates, couples into different components (e.g., photodetectors), and interacts with the materials.

- Field Visualization: Tidy3D offers visualization tools to plot the real, imaginary, or absolute values of the electric or magnetic fields. Users can slice through the simulation domain at various planes to study the field distributions at different cross-sections.

What else can be done?

- Monitor Placement: For more detailed analysis, multiple field monitors can be placed at different locations in the simulation domain. This allows for a comprehensive understanding of how the fields evolve as they propagate through the device.
- Extracting Time-Domain Data: Users can extract time-domain data from the field monitors to study the time evolution of fields at specific locations, useful for studying pulsed systems or transient phenomena.
- Power Calculations: Field monitors can be used in conjunction with flux monitors to compute the power flow through different regions of the device. This is useful for studying power coupling between components or determining the efficiency of a waveguide or photodetector.

B.8 Advanced Features and Customizations

Tidy3D offers several advanced features for users who require more complex simulations or need to model specific phenomena. Below are some additional functionalities that may be useful for future projects:

Nonlinear Materials:

Tidy3D can model nonlinear optical materials, such as those used in frequency doubling or parametric amplification. Users can define nonlinear polarization terms that account for second- or third-order nonlinear effects.

Periodic Structures:

For simulating periodic photonic structures (e.g., photonic crystals or metasurfaces), Tidy3D supports periodic boundary conditions, allowing users to model infinitely repeating unit cells. This is useful for studying the bandgap properties of periodic devices or for designing grating couplers.

Multi-Mode and Multi-Port Simulations:

Tidy3D supports multi-mode simulations, allowing users to inject multiple modes into a waveguide and study their interactions. It also supports multiple ports, enabling simulations of devices like directional couplers or multimode interferometers (MMIs).\

Parameter Sweeps:

Tidy3D allows for automated parametric sweeps, where users can vary geometric or material parameters (e.g., waveguide width, cladding thickness) and rerun the simulation to study the effect of these variations on device performance.

Optimization:

Tidy3D can be integrated with external optimization frameworks to perform automated optimization of device designs. This is useful for maximizing performance metrics, such as coupling efficiency or minimizing insertion losses.

APPENDIX C – USING SYNOPSIS RSOFT

BeamPROP BPM is a versatile tool for simulating the propagation of light in optical waveguides and photonic devices. Using the Graphical User Interface (GUI) makes it intuitive to set up simulations, adjust parameters, and visualize results without the need for scripting or command-line inputs. This appendix provides a detailed guide on how to perform simulations using the GUI.

C.1 Starting BeamPROP and Setting Up the Environment

1. Launch the RSoft CAD Environment:
    - Open the RSoft CAD software from your applications menu or desktop shortcut.
    - The main window provides access to drawing tools, simulation settings, and analysis options.
2. Create a New Design:
    - Go to File > New to create a new design.
    - Choose the appropriate units (typically micrometers) and set up the coordinate system as needed.
3. Select BeamPROP as the Simulation Tool:
    - In the top menu, click on Simulation > Global Settings.
    - In the Global Settings dialog, set the Simulation Tool to BeamPROP.

C.2 Defining the Structure and Materials

1. Draw the Structure:
    - Use the drawing tools on the left toolbar to create shapes representing waveguides, claddings, and other components.
    - Common tools include Rectangle, Polygon, Bezier Curve, and Path.
2. Assign Materials to Objects:

- Select an object in the design area.
- Right-click and choose Properties to open the object's properties dialog.
- In the Material tab, assign a material from the library or define a new one:
  - Click on Select to choose from predefined materials.
  - To create a custom material, click Edit and define the refractive index and other properties.

3. Layer Stack (for 3D Structures):
   - If you're working with a 3D structure, define the layer stack by going to Structure > Layers.
   - Add layers specifying thickness and material.

Tips:

- Grid Settings: Adjust the grid snap settings for precise drawing by going to View > Grid Settings.
- Units: Ensure that all dimensions are consistent with the chosen units (e.g., micrometers).

C.3 Setting Up Simulation Parameters

1. Open the Simulation Parameters Dialog:
   - Click on the green Perform Simulation button (looks like a traffic light) on the left toolbar.
   - This opens the BeamPROP Simulation Parameters dialog.
2. Define the Spatial Domain:
   - X Min / Max and Y Min / Max: Set the transverse boundaries of the simulation domain.
     - By default, BeamPROP automatically sets these based on your structure dimensions.
     - You can adjust them to ensure all significant fields are captured.
   - Z Start / End: Define the longitudinal extent of the simulation.

3. Set the Grid Sizes:
    - ΔX, ΔY: Set the transverse grid sizes.
        - Smaller grid sizes increase accuracy but require more computation time.
    - ΔZ: Set the longitudinal step size.
        - A smaller ΔZ improves accuracy, especially in regions where the refractive index changes rapidly.
4. Boundary Conditions:
    - Under the Boundary Conditions tab, you can choose between options like Transparent or Perfectly Matched Layer (PML).
    - For most simulations, the default transparent boundary conditions are sufficient.
5. Polarization and Wide-Angle Options:
    - Under the Options tab, select the appropriate Vector Mode:
        - Scalar (None): For simulations where polarization effects are negligible.
        - Semi-Vector TE/TM: When considering TE or TM modes separately.
        - Full-Vector: For simulations where polarization coupling is significant.
    - Wide-Angle BPM: Check this option if your simulation involves large-angle propagation or high-index contrast materials.

C.4 Defining the Source (Launch Field)

1. Set the Wavelength:
    - In the Global Settings dialog (Simulation > Global Settings), set the Wavelength parameter to your desired operating wavelength (e.g., 1.55 μm).
2. Define the Launch Field:
    - In the BeamPROP Simulation Parameters dialog, click on the Launch Field button.
    - In the Launch Field dialog:
        - Launch Type: Choose the type of source:

        - Gaussian Beam: For a free-space beam or approximating fiber coupling.
        - Mode: To launch a specific mode calculated from the structure.
        - File: To use a custom field profile from a file.
    - Polarization: Select the polarization state (e.g., TE, TM).
    - Position: Set the launch position (X, Y coordinates).
    - Orientation: Define any angle or tilt of the source if needed.
    - Parameters: Set parameters specific to the launch type (e.g., beam waist for Gaussian beams).
3. Visualize the Launch Field:
    - Click on the View button in the Launch Field dialog to see a graphical representation of the source profile.

C.5 Adding Monitors for Data Collection

1. Pathway Definition (Optional):
    - If you want to monitor the field along a specific path, define a pathway:
        - Click on the Pathways button in the left toolbar.
        - In the layout, select segments or draw a pathway where you wish to collect data.
2. Add Pathway Monitors:
    - In the BeamPROP Simulation Parameters dialog, click on the Monitors button.
    - In the Monitors dialog:
        - Click Add to create a new monitor.
        - Monitor Type: Choose from options like Power, Phase, Overlap, etc.
        - Pathway: Assign the monitor to a pathway if you have defined one.
        - Parameters: Set any specific parameters for the monitor.
3. Add Monitor Objects (Field Monitors):
    - To collect field data at specific locations:

- Use the Monitor tool from the left toolbar (looks like a small antenna or probe).
- Place the monitor in the layout where you want to record data.
- Set its properties by right-clicking and selecting Properties.

C.6 Running the Simulation

1. Review All Settings:
    - Ensure that all simulation parameters, source definitions, and monitors are correctly set.
2. Start the Simulation:
    - Click OK in the BeamPROP Simulation Parameters dialog.
    - The simulation window will open, and the simulation will begin.
    - During the simulation, a dynamic field display shows the propagation of the field along the Z-axis.
3. Monitor Simulation Progress:
    - You can observe the field distribution updating in real-time.
    - The simulation progress bar indicates the computation status.

C.7 Visualizing and Analyzing Results

1. Accessing Output Data:
    - Upon completion, BeamPROP saves output files in the specified directory.
    - The data includes field profiles, power distributions, and monitor data.
2. Using WinPLOT:
    - Click on the WinPLOT button in the top toolbar of the CAD environment.
    - In WinPLOT:
        - Open the desired output file (e.g., field profiles, monitor data).
        - Use plotting tools to visualize the data:
            - 2D/3D Plots: View cross-sectional or longitudinal field distributions.

        - Contour Plots: Visualize intensity patterns.
        - Line Plots: Analyze power or phase along a pathway.

3. Interpreting Results:
    - Field Distributions: Assess how the optical field propagates through your structure.
    - Power Monitors: Determine insertion loss, coupling efficiency, or mode conversion.
    - Phase Monitors: Useful for interferometric devices to analyze phase shifts.
4. Adjusting Display Options:
    - In WinPLOT, customize the display:
        - Change color scales.
        - Adjust axis limits.
        - Add annotations or markers.

Tips:

- Use the DataBROWSER tool to manage and organize simulation data.
- Export plots or data for use in reports or further analysis.

C.8 Advanced GUI Features

1. Parameter Scans and Optimization:
    - Use the MOST tool (Multi-variable Optimization System Technology) integrated within the GUI.
    - Set up parameter sweeps to study the effect of varying dimensions or material properties.
2. Mode Solving with the GUI:
    - Go to Simulation > Mode Calculation.
    - Set up mode-solving parameters to calculate eigenmodes of your waveguide structure.
3. Nonlinear and Anisotropic Materials:
    - Define nonlinear properties in the material editor.
    - For anisotropic materials, specify the refractive index tensor components.